Simulation Methods for Solvent Vapor Annealing of Block Copolymer Thin Films

Adam F. Hannon[a,b], Wubin Bai[a], Alfredo Alexander-Katz[a], Caroline A. Ross[a*]

[a] Department of Materials Science and Engineering, Massachusetts Institute of Technology,

77 Massachusetts Avenue, Cambridge, Massachusetts 02139

[b] Now at Materials Science and Engineering Division, National Institute of Standards and Technology,

100 Bureau Drive, Gaithersburg, MD 20899

*Address correspondence to caross@mit.edu.

Electronic Supplementary Information

S1: Experimental Details

75 kg/mol PS-PDMS thin films were spin coated on ~1 cm^2 silicon oxide substrates functionalized with hydroxyl-terminated 1 kg/mol PDMS (~2 nm thick brush layer)[1]. Various spin speeds were used to control the film thickness. A Filmetrics F20 UV-Vis spectral reflectometer was used to measure film thickness[2].

A range of volumetric mixtures of toluene and heptane solvents were used to anneal block copolymer films. These ratios included 1:0, 10:1, 5:1, 4:1, 3:1, 5:2, and 3:2. Closed reservoir annealing was used with a total reservoir volume around 80 cm^3 and the vapor pressure and evaporation rate of the liquid solvent varied by using a loose fitted lid on the reservoir. Approximately 6 cm^3 volume of solvent liquid was used in the chamber and the sample was placed above on a glass slide support above the liquid solvent. The annealing took places at a temperature of $23 \pm 2°C$ at 83% humidity. The equilibrium swelling ratio was varied using different lids and chambers which altered the partial pressures during annealing. Equilibrium swelling was normally reached after around 3 hours indicated by a plateau in film thickness and the film was slowly dried in a four step process by slowly opening the lid in four equal areas every 5 minutes for a total time of 20 minutes. Each of these quenching steps roughly corresponds to an increase in areal evaporation rate of ~3 cm^3/min. The actual rate of removal of

solvent from the substrate is within a few seconds as indicated by the colour change of the film upon the initial opening of the lid, but the four step process leads to full evaporation of the liquid reservoir.

Reactive ion etching was performed with a ~5 s CF$_4$ plasma to remove the PDMS surface layer followed by ~20 s oxygen plasma to remove the PS matrix for imaging the samples in a scanning electron microscope.

S2: Details of the SCFT Modelling

SCFT allows the numerical prediction of BCP system phase behavior under a variety of thermodynamic control variable values and boundary conditions. The effects of additional components such as solvents, homopolymers, nanoparticles, and other BCPs can all also be explored through the framework of SCFT[3–8].

The key starting point with SCFT is the polymer partition function Z. Z is a functional of a Hamiltonian H that corresponds to the free energy of the system at a given field solution. Rather than write H as a function of the positions of the monomers along the chain, one can write H as a function of density and chemical potential fields, ρ and Ω, respectively, which are functions of spatial coordinates $\vec{r} = \{x, y, z\}$. Z is then given as

$$Z = \int e^{\frac{-H[\rho,\Omega]}{kT}} D\rho D\Omega \quad \text{(ES1)}$$

where T is the temperature, k is the Boltzmann constant, and D represents integration over a function. SCFT simulations thus seek to find the set of fields ρ^* and Ω^* that satisfy the mean-field saddle point equations or SCFT conditions

$$\left.\frac{\delta H}{\delta \rho}\right|_{\rho^*} = 0 \text{ and } \left.\frac{\delta H}{\delta \Omega}\right|_{\Omega^*} = 0. \quad \text{(ES2)}$$

ρ^* and Ω^* thus represent either an equilibrium or metastable morphology the BCP can form under the specified simulation conditions. To verify this morphology solution is the global minimum structure, multiple simulations are normally performed and the energies of different saddle point solutions compared. However, non-global equilibrium structures are of interest as real systems can become kinetically trapped.

A continuous Gaussian chain model is used for the partition function since the material of interest, PS-PDMS, is a coil-coil polymer. For diblock copolymers (BCPs), the density field contribution to the partition function integrates out from the chemical potential field contribution and Z can be found as just a function of Ω. Ω consists of two independent contributions for BCPs that are factored out as Ω_+, a pressure-like field contribution, and Ω_-, an exchange interaction field contribution. H for BCPs is thus given as

$$H[\Omega_+, \Omega_-] = C\left(\int d\vec{\mathbf{r}}\left((2f-1)\,\Omega_- + \frac{\Omega_-^2}{\chi N} - \Omega_+\right) - V\ln(Q[\Omega_+, \Omega_-])\right).\ \text{(ES3)}$$

Here, χ is the Flory-Huggins interaction parameter, f is the volume fraction of the minority component, N is the degree of polymerization, V is the volume of the simulation unit cell, and C is a dimensionless concentration constant of the monomers in the polymer chain such that $C = \frac{\rho_0 R_g^3}{N}$ where ρ_0 is the density of monomer in the chain and R_g is the radius of gyration of the polymer. The single chain partition function Q under the mean field conditions is found by calculating the propagators q along the chain under the current chemical field conditions such that

$$Q[\boldsymbol{\mu}] = \frac{1}{V}\int d\vec{\mathbf{r}}\,q(\vec{\mathbf{r}}, s=1, \boldsymbol{\mu})\ \ \text{(ES4)}$$

where q is found solving the Fokker-Plank diffusion equations

$$\frac{\partial q(\vec{\mathbf{r}}, s, \boldsymbol{\mu})}{\partial s} = \frac{R_g^2}{N}\nabla^2 q(\vec{\mathbf{r}}, s, \boldsymbol{\mu}) - \boldsymbol{\mu}\big(\boldsymbol{\phi}(\vec{\mathbf{r}}, s, \boldsymbol{\mu})\big)q(\vec{\mathbf{r}}, s, \boldsymbol{\mu})\ \ \text{(ES5)}$$

with initial conditions $q(\vec{\mathbf{r}}, 0, \boldsymbol{\mu}) = 1$ where the measured position along the chain s starts at $s = 0$ in the minority (PDMS) terminal and ends at $s = 1$ in the majority (PS) terminal. The chemical potential field $\boldsymbol{\mu}$ here corresponds to either the PS or PDMS chain such that

$$\boldsymbol{\mu} = \begin{cases} \Omega_{PDMS} = \Omega_+ + \Omega_- & s < f \\ \Omega_{PS} = \Omega_+ - \Omega_- & s \geq f \end{cases}\ \text{(ES6)}$$

and the normalized densities $\boldsymbol{\phi}$ are found as follows

$$\boldsymbol{\phi}(\vec{\mathbf{r}}) = \begin{cases} \phi_{PDMS}(\vec{\mathbf{r}}) = \dfrac{\rho(\vec{\mathbf{r}})}{\rho_0} = \dfrac{1}{Q}\displaystyle\int_0^f ds\, q^\dagger(\vec{\mathbf{r}}, 1-s, \boldsymbol{\mu})\, q(\vec{\mathbf{r}}, s, \boldsymbol{\mu}) \\[4mm] \phi_{PS}(\vec{\mathbf{r}}) = \dfrac{\rho(\vec{\mathbf{r}})}{\rho_0} = \dfrac{1}{Q}\displaystyle\int_f^1 ds\, q^\dagger(\vec{\mathbf{r}}, 1-s, \boldsymbol{\mu})\, q(\vec{\mathbf{r}}, s, \boldsymbol{\mu}) \end{cases}\ \text{(ES7)}$$

with the backward propagator $q^\dagger$ being calculated using by solving the Fokker-Planck diffusion equation starting at the $s = 1$ (PS) end of the chain. The Fokker-Planck equation can be solved in many different ways, with a pseudo-spectral method being chosen for convenience, speed, stability, and no *a priori* assumptions needed on for the space groups in a given morphology solution[4].

    To start a simulation, an initial guess solution or random field values are assigned to Ω_-. The SCFT equations are then solved iteratively finding new values for Ω_- and Ω_+ using a steepest descent complex Langevin relaxation scheme. Using the SCFT condition

$$\left.\frac{\delta H}{\delta \Omega}\right|_{\Omega^*} = 0, \qquad \text{(ES8)}$$

a time evolution scheme of the fields is developed as follows

$$\frac{\delta \Omega_+}{dt} = \lambda_+ \frac{\delta H}{\delta \Omega_+} \text{ and } \frac{\delta \Omega_-}{dt} = \lambda_- \frac{\delta H}{\delta \Omega_-} \quad \text{(ES9)}$$

where the constants λ_+ and λ_- are chosen to be large enough to make the system converge fast in as few iterations as possible but small enough to ensure the simulation is numerically stable. Each time step t corresponds to one forward simulation iteration. In the simulations performed in this study, time constant values were chosen as $\lambda_+ = 5.0$ and $\lambda_- = 0.0033$ through computational optimization trial and error. For the BCPs studied, the analytical expressions for these derivatives using the functional form of H are given as

$$\frac{\delta \Omega_+}{dt} = \lambda_+ C (1 - \phi_+) \text{ and } \frac{\delta \Omega_-}{dt} = -\lambda_- C \left(2f - 1 - \phi_- - \frac{2\Omega_-}{\chi N}\right) \quad \text{(ES10)}$$

or rewritten in terms of iteration numbers

$$\Omega_{+,j+1} = \Omega_{+,j} + \lambda_+ C \left(1 - \phi_{+,j}\right)$$
$$\Omega_{-,j+1} = \Omega_{-,j} - \lambda_- C \left(2f - 1 - \phi_{-,j} - \frac{2\Omega_{-,j}}{\chi N}\right) + \lambda_- \eta(\vec{\mathbf{r}}) \qquad \text{(ES11)}$$

where the jth iterations is denoted by j. The term $\eta(\vec{\mathbf{r}})$ is Gaussian distributed random noise added to the second update scheme equation for Ω_- in complex Lagevin dynamics that keeps the system out of shallow metastable solutions. SCFT simulations are normally performed on a discrete grid of size N_x by N_y by N_z points with each point corresponding to a location in real

space. The number and size are chosen based on coarse-graining considerations as well as expectations of symmetries for unit cell calculations. Boundary conditions to enforce different surface wetting conditions are added by constraining the appropriate field values to stay constant at the interfaces. These conditions amount to having large Ω_+ constraints at hard interfaces and negative values of the appropriate Ω field for PS or PDMS to attract a given polymer species for preferential surfaces. The actual values used are based on previous work[8,9].

S3: Effective Fraction Fit

Modelling the PS-PDMS solvent annealing with selective solvents toluene and heptane requires the accurate estimation of the effective control variables of the system, χ_{eff} and f_{eff}. χ_{eff} depends on the fraction of incorporated solvent Φ_{sol} or simply the inverse of the swelling ratio S_R. However, most BCP morphologies vary little with changing χ except when the weak segregation regime is approached. Thus in simulations usually just choosing a few representative χ values to test allows one to get a general sense of what the actual χ_{eff} is for comparison with experiments. Estimating f_{eff} from experiment is more difficult though, since the solvents used are not mutually selective to the two blocks and thus dividing the solvent into the appropriate phase regions in the film cannot be directly inferred from experiment. To find the best way of calculating f_{eff}, two simple extreme models for the heptane and toluene system are first examined and then compared with a composite model based on homopolymer thin film swelling experiments from a previous study[10]. In this previous study, toluene was found to be slightly preferential to PS or neutral while heptane was very preferential to PDMS. Using these observations, the first extreme model (denoted Model 1) makes the assumption that 50% of the toluene in the swollen film enters the PDMS domains and 50% of the toluene enters the PS domains, and heptane swells only the PDMS domains. The 50% assumption is independent of PDMS volume fraction. To contrast this model, the extreme case where toluene is fully preferential to PS is considered (denoted Model 2). Experimentally this can occur when both heptane and toluene are present in the film in large concentrations with the heptane forcing the toluene to selectively swell only the PS.

The effective fraction for Model 1 is thus given in terms of the bulk PDMS volume fraction f, fraction of heptane solvent in the film θ_{hept}, and fraction of toluene solvent in the film θ_{tol} as

$$f_{eff1} = fS_R^{-1} + \left(\theta_{hept} + \frac{\theta_{tol}}{2}\right)(1 - S_R^{-1}) \quad \text{(ES12)}$$

and for Model 2 as

$$f_{eff2} = fS_R^{-1} + \theta_{hept}(1 - S_R^{-1}). \quad \text{(ES13)}$$

Here $\theta_{hept} + \theta_{tol} = 1$ as the total fraction of all solvent types in the swollen film should be unity. A third model (denoted Model 3) is a general model that allows for a selectivity coefficient ζ that is a function of θ_{hept} and θ_{tol} and is given as

$$f_{eff3} = fS_R^{-1} + \zeta(\theta_{tol}, \theta_{hept})(1 - S_R^{-1}). \quad \text{(ES14)}$$

Model 3 thus accounts for the non-ideal and nonlinear behavior between heptane and toluene[11].

$\zeta(\theta_{tol}, \theta_{hept})$ can be determined by estimating f_{eff} from actual experimental data. While using only the swelling data of BCP films does not allow for such an estimation, combining BCP film swelling data with homopolymer swelling data can in principle give a decent estimation for f_{eff} as follows: The bulk dry film volume fraction is written $f = \frac{V_{PDMS}}{V_0}$ in terms of the initial volume of the thin film V_0 and volume of PDMS in the dry film V_{PDMS}. The PDMS effective volume fraction when swollen can then be written $f_{eff} = \frac{(V_{PDMS} + V_{sol})}{V_S}$ in terms of the swollen film volume V_S and volume solvent present only in PDMS features V_{sol} in addition to V_{PDMS}. By dividing the equation for f_{eff} by f, the relationship is found $f_{eff} = f\left(\frac{V_{PDMS} + V_{sol}}{V_{PDMS}}\right)\frac{V_0}{V_S}$. Here the fraction $\frac{V_0}{V_S}$ is simply the inverse of the swelling ratio of the BCP film $S_{R,BCP}$ such that $\frac{V_0}{V_S} = S_{R,BCP}^{-1}$. The fraction $\frac{V_{PDMS} + V_{sol}}{V_{PDMS}}$ can be estimated from the swelling ratio of pure PDMS thin film $S_{R,PDMS}$ (the limit where $f_{eff} = f = 1$) such that $\frac{V_{PDMS} + V_{sol}}{V_{PDMS}} \cong S_{R,PDMS}$. Fitting the data from the previous study[10] using the swelling data PDMS and PS homopolymer thin films with the PS-PDMS thin film data, a fit for ζ using the form

$$\zeta(\theta_{tol}, \theta_{hept}) = \beta_{tol}(\theta_{tol})\theta_{tol} + \beta_{hept}(\theta_{tol})\theta_{hept} \quad \text{(ES15)}$$

with $\beta_{hept}(\theta_{tol})$ and $\beta_{tol}(\theta_{tol})$ as best fit functions was found. These two fit functions are plotted as a function of θ_{tol} in Figure S1.

The original study presented swelling ratios as a function of y_{tol}, the mole fraction toluene in the vapor. Since equilibrium is assumed to be met for the measured swelling ratios, the assumption is made that $y_{tol} \cong \theta_{tol}$ in this data fit. From the plots, the observation is made that β_{hept} is almost equal to 1 for all θ_{tol} while β_{tol} is almost equal to 0 for low θ_{tol} and increases linearly to ≈ 0.25 for $\theta_{tol} > 0.7$ meaning toluene is selective to PS when heptane is in the film but does swell PDMS somewhat when less heptane is present. This means the real system's Model 3 is closer to Model 2 for $\theta_{tol} < 0.7$ and somewhere between Model 1 and 2 for $\theta_{tol} > 0.7$ as the toluene is never completely neutral to the two blocks.
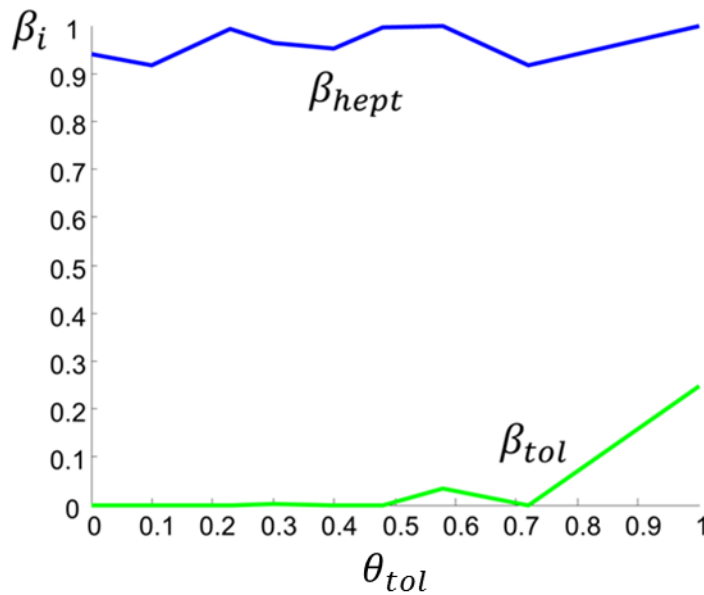
Figure S1: Plots of the β fit parameters for Model 3 versus θ_{tol}. β_{hept} is shown in blue and β_{tol} is shown in green.

To better compare the three models 1, 2, and 3, plots of f_{eff1}, f_{eff2}, and f_{eff3} respectively as a function of θ_{tol} for fixed values of S_R and two f volume fractions ($f = 0.33$ corresponding to the 45.5 kg/mol PS-PDMS used in the previous study[10] and $f = 0.41$ corresponding to the 75 kg/mol PS-PDMS) are shown in Figure S2. The values for f_{eff3} will provide the best fit to the experimental system, and f_{eff1} and f_{eff2} provide limiting cases such that $f_{eff} \cong f_{eff_2}$ for lower θ_{tol} and $f_{eff} \cong f_{eff_1}$ for higher θ_{tol}. f_{eff_3} does indeed approach f_{eff_2} for low θ_{tol} but does not quite reach the f_{eff_1} limit as shown in Figure S2.
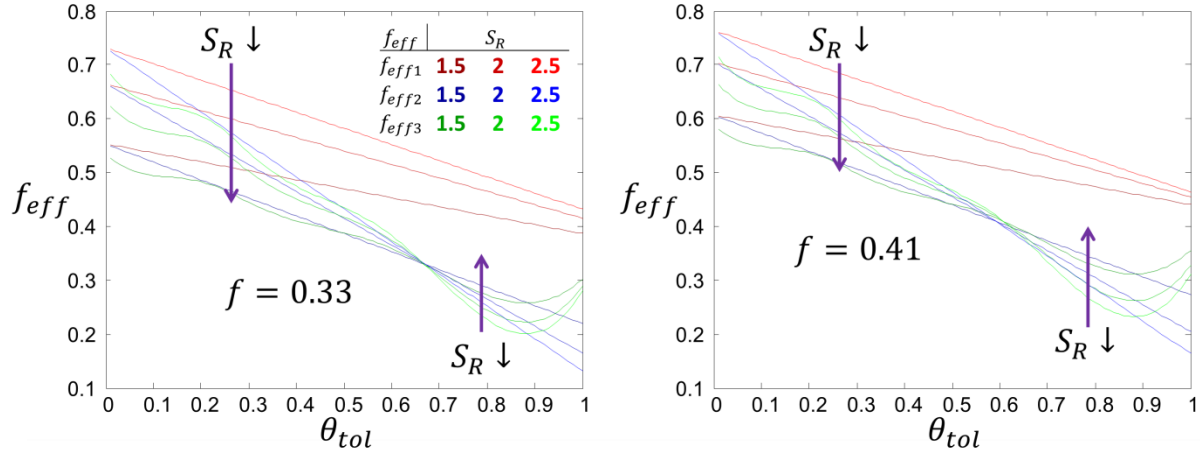
Figure S2: f_{eff} plotted versus θ_{tol} for $f = 0.33$ (left) and $f = 0.41$ (right) for three swelling ratios $S_R = 1.5, 2,$ and 2.5. Model 1 f_{eff_1} is shown in shades of red, Model 2 f_{eff_2} is shown in shades of blue, and Model 3 f_{eff_3} is shown in shades of green

In the main text, Model 3 was used for comparing simulation results with experiments. There $\alpha(\theta_{tol}, \theta_{hept})$ is replaced with $\xi_{A,sol}$ in the context of the SCFT model with species A and B instead of PDMS and PS. Everything else in the model remains the same.

S4: Simulation-Experiment Comparison

In order to compare the simulation results with experimental results, the simulation variables need to be correlated to the experimental parameters with care. The experimental determination of microdomain morphology is based on etched samples after quenching whereas the implicit simulation results represent the morphology present before quenching the system. To account for this we assume that upon quenching, the morphologies in the simulation will be collapsed in the thickness direction by a factor approximately equal to $1/S_R$ assuming $D_0 = D_f$. If the solvent selectivity is such that f_{eff} is very different from the bulk BCP f, there will also be some lateral shrinkage or growth of the minority features for $f_{eff} > f$ and $f_{eff} < f$, respectively. The presence or absence of a minority wetting surface layer that depends on the solvent preferentiality will affect the absolute S_R at which commensurate morphologies are observed. The etching process itself may disturb the shape and size of the microdomains. Further, nonequilibrium processes such as film dewetting compete with the desired BCP microphase segregation, and kinetically trapped morphologies or local defects are expected in experiments. In the modelling, we therefore explore ranges of f_{eff}, χ_{eff}, and S_R to illustrate trends in the morphologies and give a qualitative comparison with experiment.

S5: Bulk Equilibrium Structure Simulations and Effective χN

Before considering thin film simulations, an examination of bulk behavior of the BCP in simulations was performed using the appropriate volume fraction of the gyroid-forming BCP at $f = 0.411$. Three effective Flory-Huggins parameters of $(\chi N)_{eff} = 14, 18,$ and 30 were examined which fall near the lower end of the range of $(\chi N)_{eff}$ for the swelled 75.5 kg/mol BCP. Using a reduced degree of polymerization $N = 125$ in the model (based on using Kuhn segments rather than chemical repeat units in the SCFT) and taking $\chi = 0.27$, these would roughly correspond to swelling ratios of $S_R = 2.4, 1.9,$ and 1.1, respectively, for a thin film system. Fully periodic cubic unit cells with grid size $N_x = N_y = N_z = 16$ were performed with the side length of the unit cell varied from $2.43R_g$ to $7.30R_g$ in order to find the equilibrium lengths of the morphologies observed, where R_g is the radius of gyration of the BCP. In these simulations, square packed cylinders, hexagonally packed cylinders, cubic gyroid structures, and double gyroid structures were all observed depending on the unit cell side length. Representative minority density isosurfaces results of these morphologies are shown in Figure S3.

In order to compare these morphologies, free energy curves for each were calculated as a function of the unit cell side length by holding the density fields constants in additional SCFT simulations, allowing the corresponding chemical potential fields to develop, and calculating the energies at those field solutions. These free energy curves are shown in Figure S4, S5, and S6 for $(\chi N)_{eff} = 14, 18,$ and 30, respectively. For $(\chi N)_{eff} = 14$, cylinders had the lowest free energy while for the higher $(\chi N)_{eff}$ the gyroid structures became favored with lower free energy. Since the system of interest is bulk gyroid, the thin film implicit simulation studies used the lowest $(\chi N)_{eff} = 18$ since gyroid was the dominant structure, and the corresponding $S_R \cong 2$ was used to obtain that effective interaction parameter. Additionally, the hexagonal cylinder phase was found to have a minimum free energy at a close packed spacing of $5.27R_g$ and thus this value was used as L_0 for the length scale in the thin film simulations since it is a simpler measure of periodicity in the BCP system than lengths in the gyroid unit cell and corresponds better to a commensurate monolayer length in thin films.
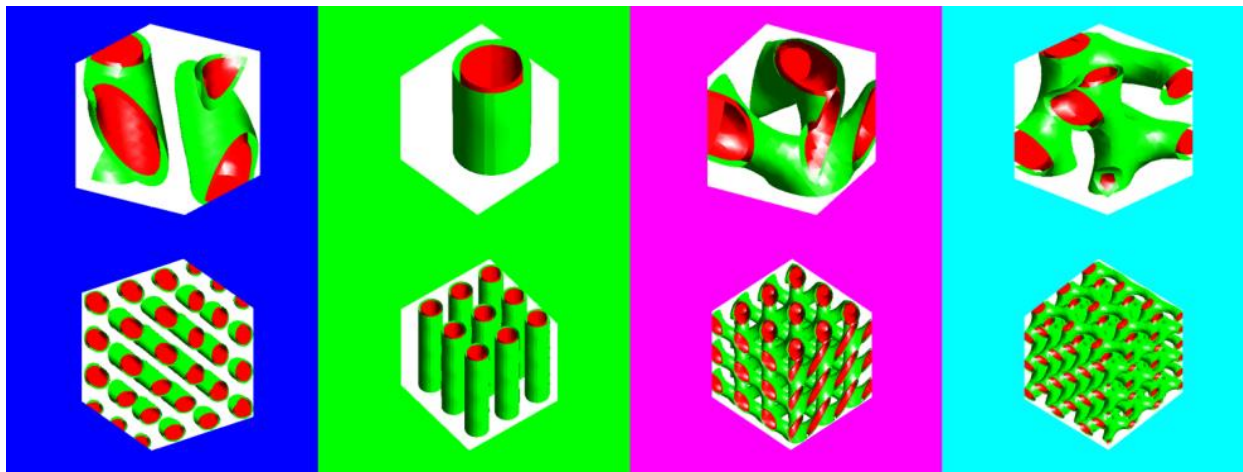
Figure S3: Bulk equilibrium morphologies observed in SCFT simulations. $\phi = 0.5$ minority isosurfaces density regions are coloured green with red regions being the minority rich regions. The top structures are single unit cells and the bottom structures are three unit cells repeated in each direction for extended clarity of the structure (total of 27 unit cells). (Left) Hexagonally packed cylinders. (Middle Left) Square packed cylinders. (Middle Right) Cubic gyroid. (Right) Double gyroid.
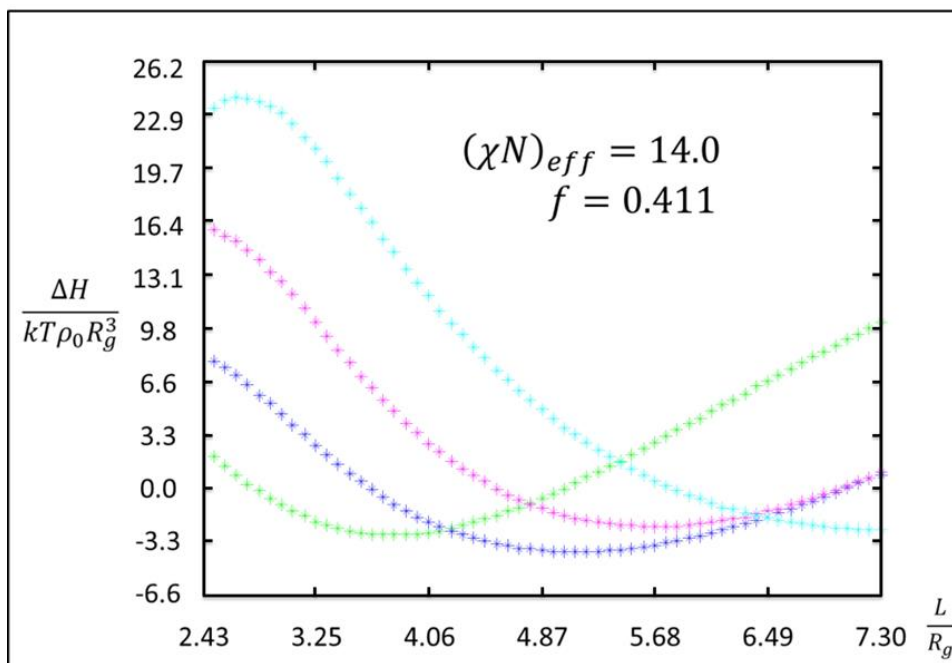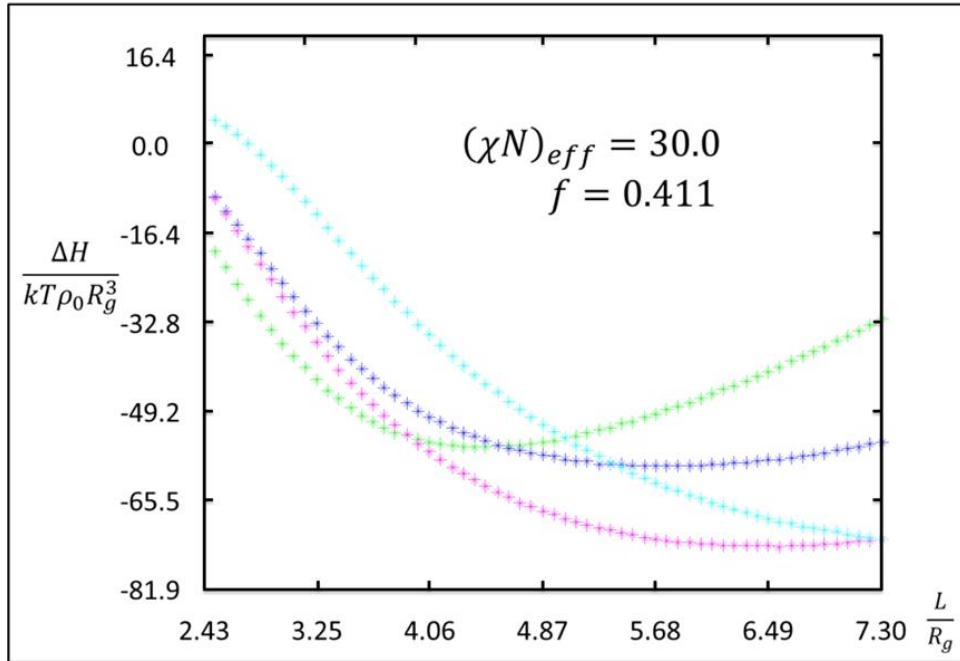

Figure S4: Plots of the normalized free energies relative to a disordered melt of the simulated SCFT equilibrium structures colour coded to match those in Figure S3 (i.e. dark blue: hexagonally packed cylinders; green: square packed cylinders; magneta: cubic gyroid; light blue: double gyroid) for $(\chi N)_{eff} = 14$ and $f = 0.411$.
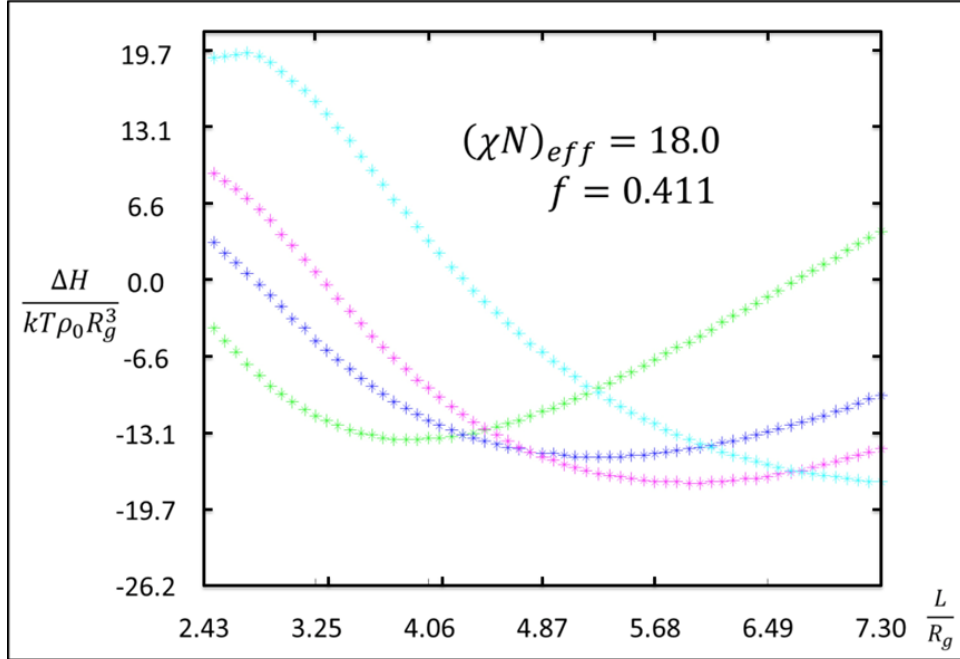
Figure S5: Plots of the normalized free energies relative to a disordered melt of the simulated SCFT equilibrium structures colour coded to match those in Figure S3 (i.e. dark blue: hexagonally packed cylinders; green: square packed cylinders; magneta: cubic gyroid; light blue: double gyroid) for $(\chi N)_{eff} = 18$ and $f = 0.411$.

Figure S6: Plots of the normalized free energies relative to a disordered melt of the simulated SCFT equilibrium structures colour coded to match those in Figure S3 (i.e. dark blue: hexagonally packed cylinders; green: square packed cylinders; magneta: cubic gyroid; light blue: double gyroid) for $(\chi N)_{eff} = 30$ and $f = 0.411$.

S6: Full Set of Thin Film Simulations Performed

The thin film simulations used periodic boundary conditions in the in-plane x and y directions and used hard wall boundary conditions with preferential surface wetting layers in the out-of-plane z direction. The unit cells used had a grid size of $N_x = 32, N_y = 28,$ and $N_z = 18$. The x and y side lengths were non-integer multiples of L_0 such that the unit cell diagonal dimension was also non-integer. This avoids a bias towards forming specific commensurate morphologies. An alternative approach would have been to use a much larger unit cell, but this would have required longer computational time. The film thickness t was varied from $1.62R_g$ to $8.11R_g$ with $(\chi N)_{eff} = 18.0$.

To examine different selective solvent ratio conditions, four effective fractions were used with values $f_{eff} = 0.25, 0.35, 0.41,$ and 0.45. The complete phase diagram results for these four effective fractions are shown in Figures S7, S8, S9, and S10 with colour coding that corresponds to the free energy diagrams in the main text Figure 4.
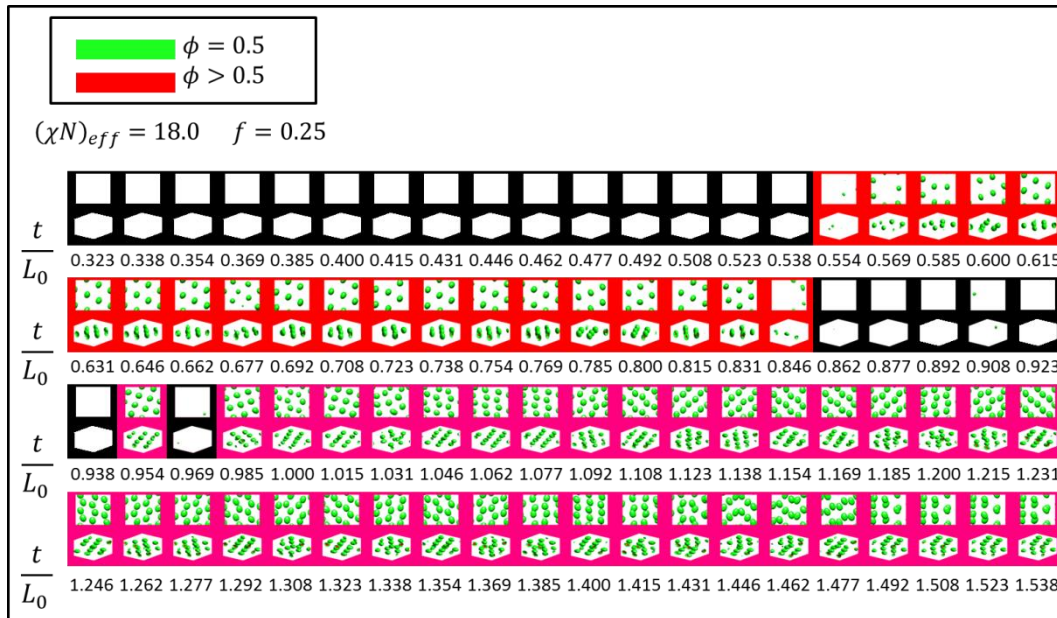

Figure S7: Thin film equilibrium morphologies observed in SCFT simulations as a function of normalized thickness $\frac{t}{L_0}$ for $f_{eff} = 0.25$. Structures include spheres (red background) and double layers of spheres (pink).
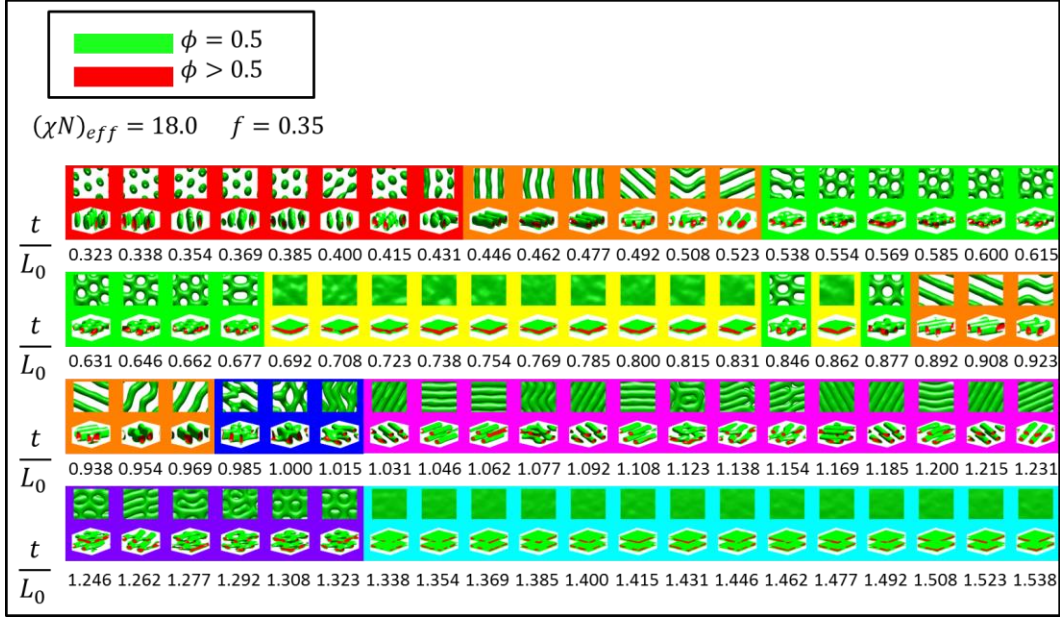
Figure S8: Thin film equilibrium morphologies observed in SCFT simulations as a function of normalized thickness $\frac{t}{L_0}$ for $f_{eff} = 0.35$. Structures include spheres (red), perforated lamellae (green), cylinders (orange), lamellae (yellow), and double layered structures (blue, magenta, purple, light blue).
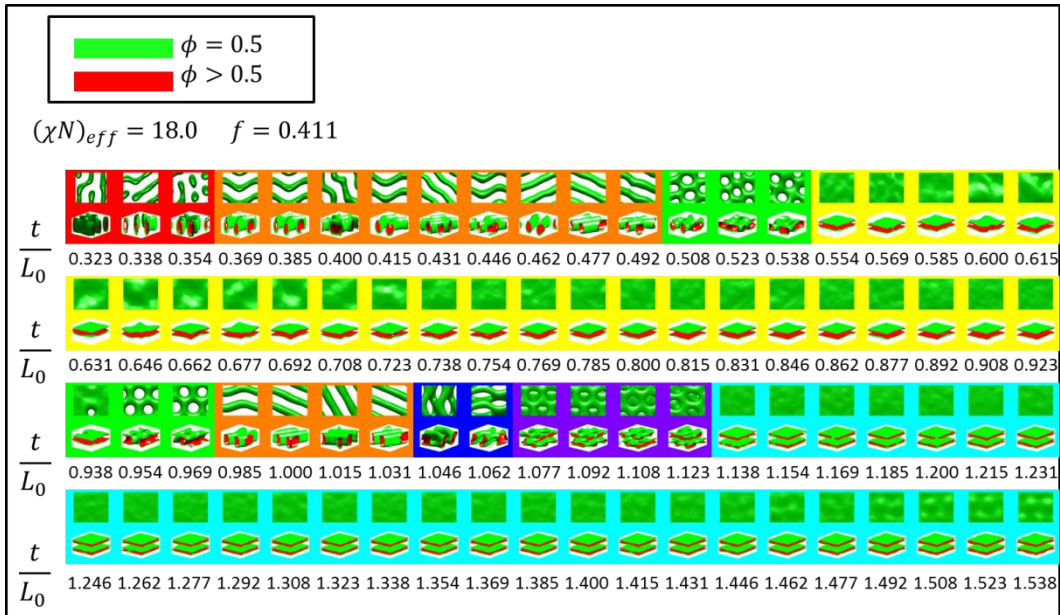

Figure S9: Thin film equilibrium morphologies observed in SCFT simulations as a function of normalized thickness $\frac{t}{L_0}$ for $f_{eff} = 0.411$. Structures include perforated lamellae, cylinders, lamellae, and double layered structures.
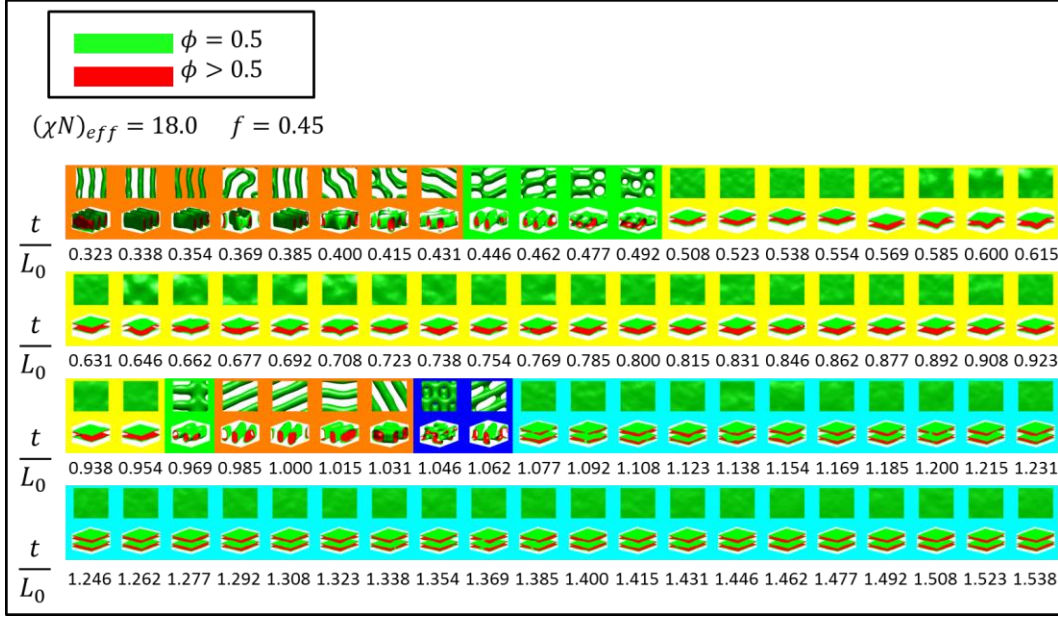
Figure S10: Thin film equilibrium morphologies observed in SCFT simulations as a function of normalized thickness $\frac{t}{L_0}$ for $f_{eff} = 0.45$. Structures include perforated lamellae, cylinders, lamellae, and double layered structures.

S7: Comparison of Implicit Thin Film Simulations with Previous Studies

Since the implicit thin film simulations are equivalent to the standard BCP SCFT model, the results can be compared to previous thin film simulation studies. Previous work by Li et al[12] produced a phase diagram of BCP morphologies as a function of normalized film thickness t/R_g and volume fraction f. A comparison of their phase diagram with our results for the four f examined is shown in Figure S11. In the figure, the approximate phase boundaries found by Li et al are shown as dashed lines and their letter coding for different morphologies are represented by similar letter coding that they used (S_1 for a single layer of close-packed spheres, S_2 for double layers of close-packed spheres, SC for a single layer of close-packed spheres elongated in the out-of-plane direction, C_1 for a single layer of cylinders, C_2 for a double layer of cylinders, $C_\perp$ for out-of-plane oriented cylinders connecting to the surface layers, PL_1 for a single layer of perforated lamellae, PL_2 for a double layer of perforated lamellae, $L_\perp$ for out-of-plane standing lamellae, $L_{\parallel,\perp}$ for out-of-plane lamellae not connected to the surface layer, L_1 for a single layer of in-plane lamellae, and L_2 for double layers of in-plane lamellae).The morphologies found in our simulations are shown as colour coded symbols with colours analogous to those of representative morphologies in Figures S7 through S10.

A few differences in our simulations and those of Li should be noted: Li used a higher χN value of 20 whereas our χN was 18; they modeled preferential surfaces as an exponential decay function with average strength of $0.22\chi N$ whereas we used a step function potential with strength value of $0.56\chi N$ which results in much higher preferentiality for the majority block (this corresponds in our simulations to a fixed Ω_- value of 10 versus average value in Li's simulations of ≈ 4.4, so over a factor of 2 times more preferential in our simulations); Li's phase diagram is a result of comparing the minimum free energy of all the candidate morphologies for the phase space explored whereas we found the morphologies from forward steepest decent simulations meaning some morphologies may be local equilibrium solutions rather than global solutions. Taking these differences into account and comparing the observed morphologies with their phase diagram, the results show qualitative similarities with many phase regions and transition boundaries overlapping..

For the morphologies with $f = 0.25$, disordered homogenous internal structure (black stars) (i.e. wetting layer only) is observed as opposed to a single layer of spheres which is likely due to the higher surface preferentiality in our simulations. As the film thickness increases, the single layer of spheres (red circles) appears in the region that the single layers of cylinders appeared in Li's simulations, likely due to our lower χN in conjunction with the higher surface preferentiality. Upon further increase in thickness, the region with double layers of spheres (pink circles) appears instead of Li's region of double layers of cylinders, again likely due to the slightly lower χN and higher surface preferentiality.

For the $f = 0.35$ morphologies, spheres (red circles) appear in the region where Li observed perpendicular cylinders connected to the surface. Due to the higher surface preferentiality in our simulations, spheres connected to the surface were never observed. The single layer of perforated lamellae (green plus signs) and single layer lamellae (yellow squares) fall in the expected regions from Li's model. Transitional bicontinuous cylinders (blue squares) and double layers of cylinders (magenta stars) appear around the $L_{\parallel,\perp}$ region, again likely due to the stronger surface preferentiality and lower χN. Double layer perforated lamellae (purple plus signs) and double layer in-plane lamellae (cyan squares) both appear near their predicted regions.

For the higher $f = 0.41$ and 0.45 morphologies, the thickest films showed double layer parallel lamellae (cyan squares) in the predicted region. Decreasing the thickness, double layer perforated lamellae (purple plus signs) appeared as well as bicontinous cylinders (blue squares)

and single layer cylinders (orange stars), instead of the expected $L_{\parallel,\perp}$. Decreasing thickness further, single layer lamellae (yellow squares) agreed with Li's model. The lowest thickness phases here were primarily single layer cylinders (orange stars) in a region where perpendicular standing lamellae were predicted. The stronger surface preferentiality is likely the primary factor in this observed difference, destabilizing standing lamellae.

Overall our simulation results agree quite well with Li et al. All the observed differences are reasonably explained by the higher surface boundary preferences coupled with the lower χN, with the additional possibility of some phases being local equilibrium structures.
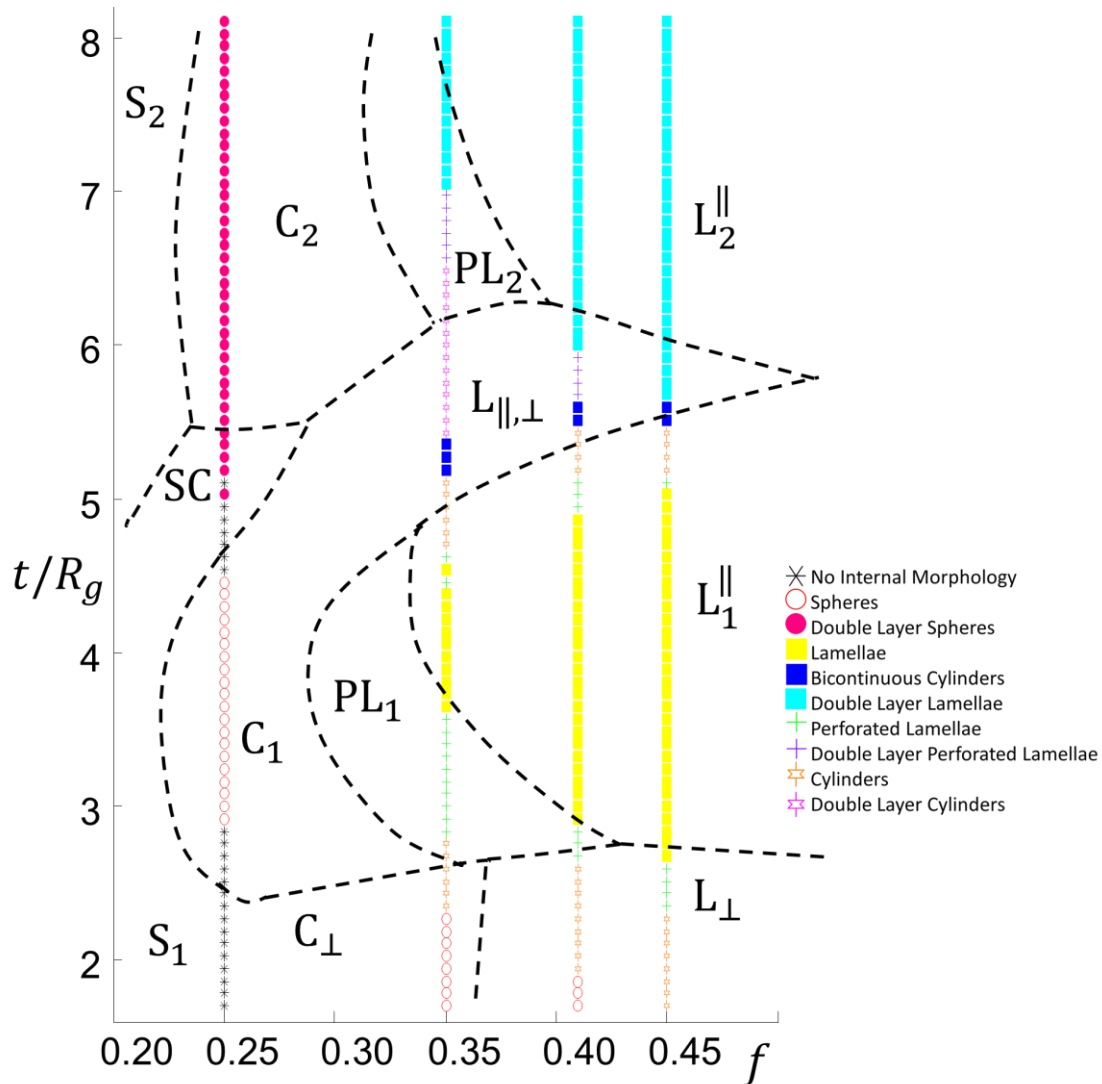

Figure S11: Results of thin film equilibrium morphologies observed in SCFT simulations overlaid on a phase diagram from a previous confined thickness simulation study of Li et al., the main differences being that our simulations have twice the surface preference for the majority block and a slightly lower $\chi N = 18$. Dashed lines indicate calculated phase boundaries from Li et al. Superposed are data points from our study, colour coded to match figures S7 through S10 with * being no internal morphology, O being spheres, + being perforated lamellae, stars being cylinders, and squares being either in-plane lamellae or bicontinuous cylinders.

16

S8: Comparison of Implicit and Explicit Models – 2D Phase Diagram

In order to more accurately compare the morphologies predicted by the implicit and explicit solvent SCFT models as well as determine how well the models compare with experimental conditions, additional simulations were performed in 2D over a range of χN, f, f_{solA}, and f_{solB}. For the case that $f_{solA} = f_{solB} = 0$, this corresponds to the standard BCP model which is also the implicit model where χ and f are mapped to their appropriate χ_{eff} and f_{eff} parameters. Simulations were performed on unit cells with size roughly $2L_0$ by $2L_0$ (depending on the morphology at those conditions). χN was varied with values 12, 14, 16, 18, 20, 24, 28, and 32. f was varied with values 0.25, 0.29, 0.33, 0.38, 0.42, 0.46, and 0.50. f_{solA} and f_{solB} were both varied over a range of values from 0 to 0.60 in steps of 0.05 in a similar fashion to those shown in the main text in Figure 5 (where in the main text $f = 0.40$ and $\chi N = 28$ but here many more values were examined and unit cells were a larger $4L_0$ by $4L_0$).

From these simulations, various phases were observed consistent with previous studies of BCP systems. These phases are detailed with representative density profiles in Figures S12 through S15. The simulation parameters where the example density profiles were obtained are detailed in the figure captions. Phase diagrams for constant total solvent volume fraction (i.e. $f_{solA} + f_{solB} = \Phi_{sol} = Constant$) for $\Phi_{sol} = 0, 0.05, 0.10, 0.15, 0.20, 0.25,$ and 0.30 are shown in Figures S16 through S22. For the cases with $\Phi_{sol} > 0$, a side by side comparison phase diagram is presented where the data is replotted with $\chi_{eff} = \chi(1 - \Phi_{sol})^\alpha$ with $\alpha = -1$ for a theoretical case of the explicit preferential solvent increasing the effective χ_{eff}. In the phase diagrams, curves representing the approximate boundaries between disordered, spherical, cylindrical, and lamellar morphologies are shown as guides.

In 2D, certain observed phases can correspond to different cross-sections of normal 3D morphologies, thus one should take care when comparing these simulations to the theoretical phase diagram for bulk BCPs. Circular structures in 2D can correspond to both spheres and cylinder cross-sections in 3D; similarly line structures can correspond to cross-sections of either cylinders or lamellae. From the phase diagrams, the morphologies observed for the implicit model or standard BCP model fall right within ranges expected from previous studies[3]. As Φ_{sol} is increased, using the input χN values as a guide, the range for observing sphere-like morphologies appears to go out into the normally disordered region. If a higher χ_{eff} is assumed in these cases, the phase diagram appears to start overlaying the standard phase diagram again,

although an exact match is not observed or expected for all cases. In particular, as the ratio of solvent in the system increases above Φ_{sol} =0.30, more two phase morphologies begin to appear where solvent no longer coexists homogeneously with the BCP. In these cases, morphologies such as micelles and vesicles of various shapes and sizes begin to appear. Since the BCP and solvent density profile no longer coexist spatially in these regions, the results in these regions cannot be taken for quantitative accuracy due to the mean field approximation breaking down for pure solvent (i.e. as long as the solvent is well dispersed in the BCP regions, the simulations give insightful results, but once macrophase segregation of solvent and BCP occur the model breaks down and only qualitative behavior can be deduced from the results).
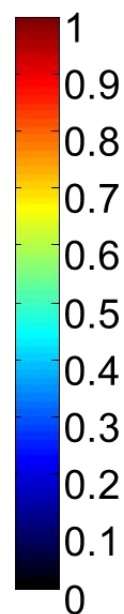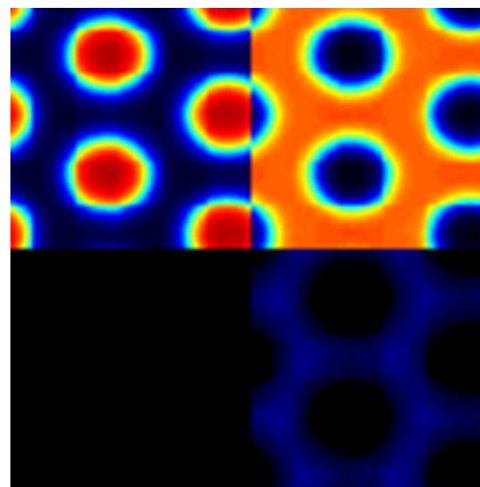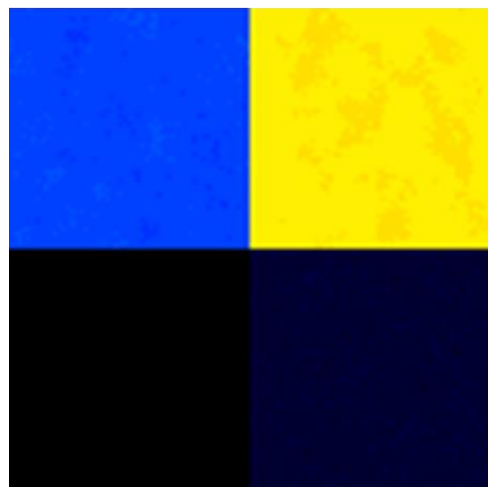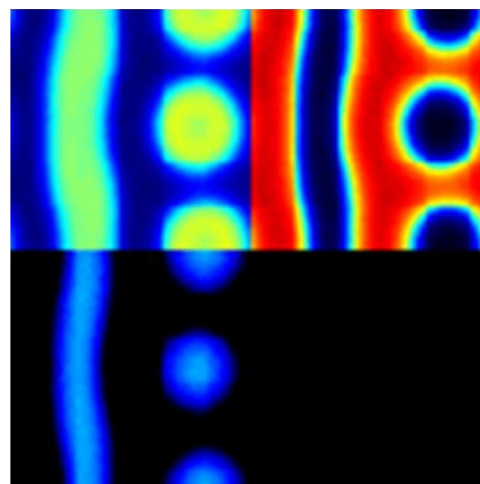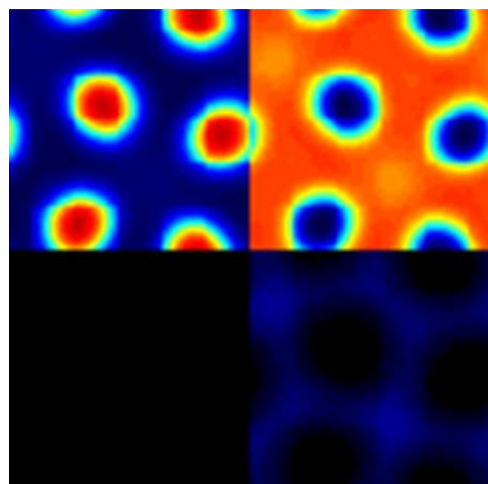
Figure S12: Example 2D density profiles of phases observed in explicit solvent simulations. Profiles are arranged with normalized A block densities in the upper-left corner, B block densities in the upper-right corner, A solvent densities in the lower-left corner, and B solvent densities in the lower-right corner. Colour bar scale is on the right. For the following, the simulation parameters in parentheses are for the particular example morphologies shown. In general these morphologies occurred over a range of parameters as detailed in the phase diagrams in Figures S16 through S22. (Top Left) Disordered homogenous phase ($f = 0.29 \; \chi N = 12 \; \Phi_{sol} = f_{solB} = 0.05 \; f_{eff} = 0.2755$). (Top Right) Close-packed circle phase ($f = 0.38 \; \chi N = 18 \; \Phi_{sol} = f_{solB} = 0.05 \; f_{eff} = 0.361$). (Bottom Left) Circular phase ($f = 0.29 \; \chi N = 18 \; \Phi_{sol} = f_{solB} = 0.05 \; f_{eff} = 0.2755$). (Bottom Right) Mixed line and circle phase ($f = 0.38 \; \chi N = 12 \; \Phi_{sol} = f_{solA} = 0.10 \; f_{eff} = 0.442$).
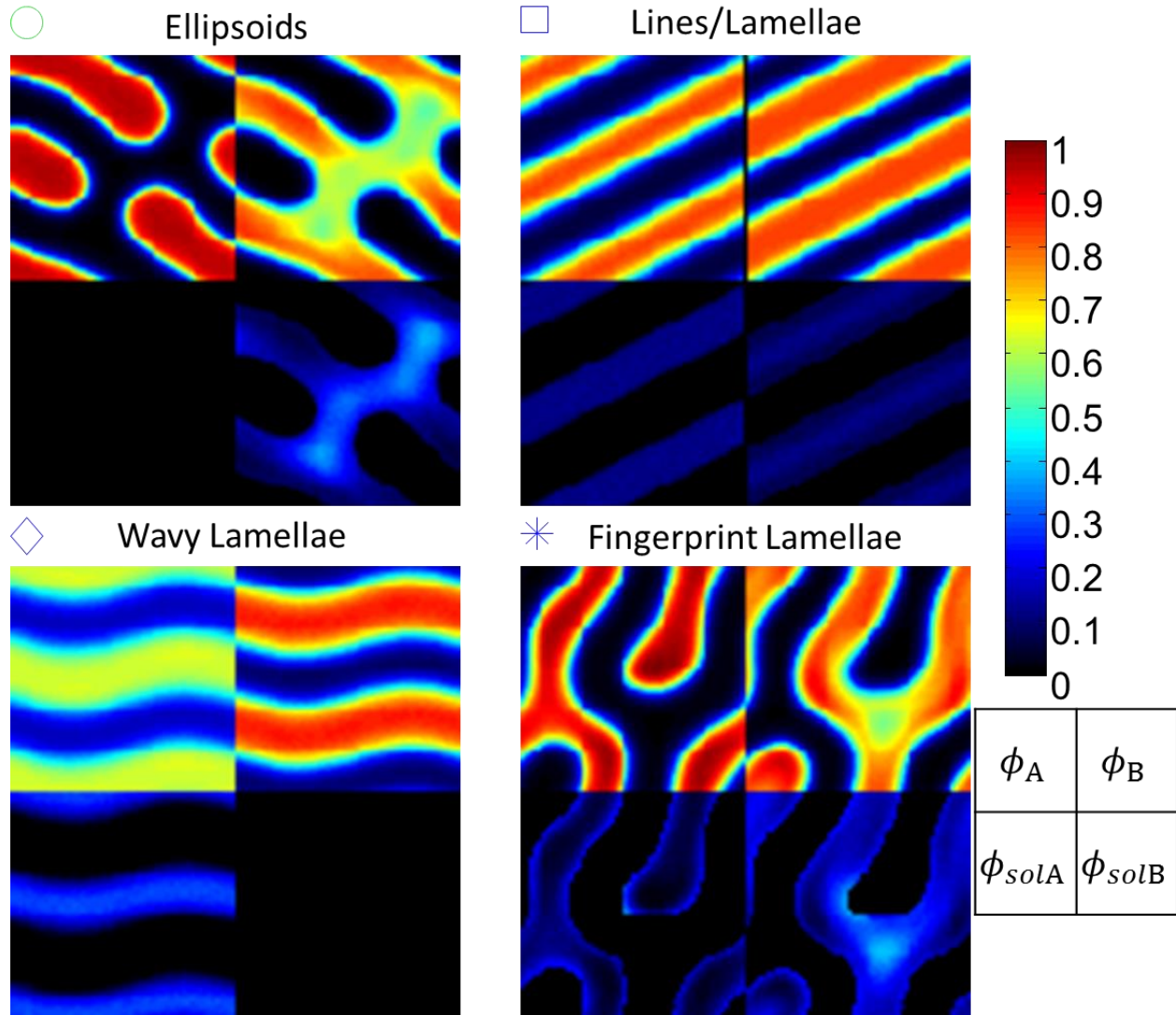
Figure S13: (Top Left) Ellipsoidal phase($f = 0.50$ $\chi N = 28$ $\Phi_{sol} = f_{solB} = 0.10$ $f_{eff} = 0.45$). (Top Right) Lines phase ($f = 0.46$ $\chi N = 16$ $f_{solA} = f_{solB} = 0.05 \rightarrow \Phi_{sol} = 0.10$ $f_{eff} = 0.464$). (Bottom Left) Wavy lines phase ($f = 0.46$ $\chi N = 12$ $\Phi_{sol} = f_{solA} = 0.10$ $f_{eff} = 0.514$). (Bottom Right) Fingerprint pattern phase ($f = 0.50$ $\chi N = 24$ $f_{solA} = 0.05$ & $f_{solB} = 0.10 \rightarrow \Phi_{sol} = 0.15$ $f_{eff} = 0.475$).
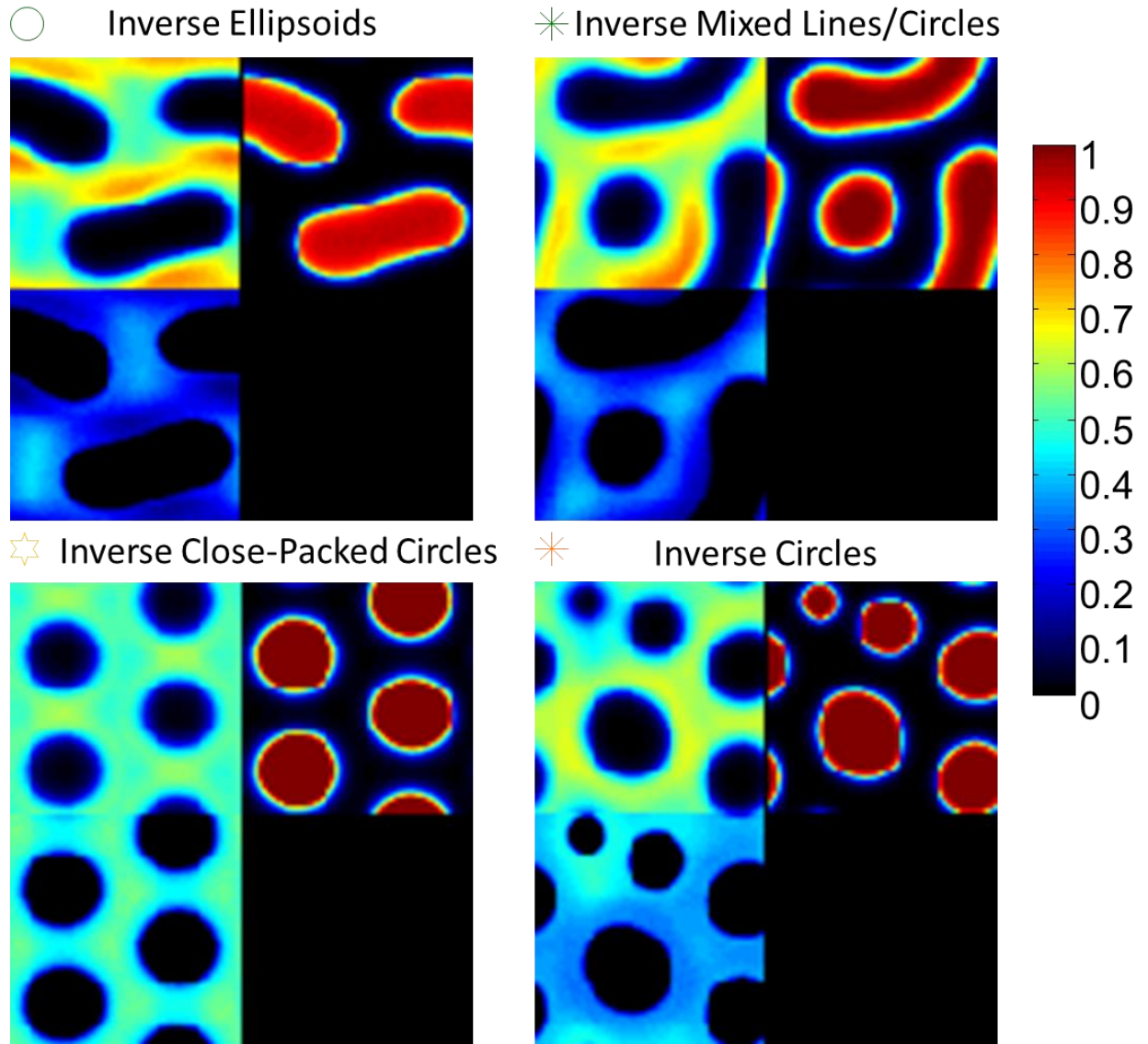
Figure S14: (Top Left) Ellipsoidal phase with B block ($f = 0.50$ $\chi N = 32$ $\Phi_{sol} = f_{solA} = 0.15$ $f_{eff} = 0.575$). (Top Right) Mixed line and circle phase with B block ($f = 0.46$ $\chi N = 20$ $\Phi_{sol} = f_{solA} = 0.15$ $f_{eff} = 0.541$). (Bottom Left) Close-packed circle phase with B block ($f = 0.46$ $\chi N = 20$ $\Phi_{sol} = f_{solA} = 0.30$ $f_{eff} = 0.622$). (Bottom Right) Circular phase with B block ($f = 0.50$ $\chi N = 32$ $\Phi_{sol} = f_{solA} = 0.25$ $f_{eff} = 0.625$).

Two Phase Morphologies (Solvent Macrophase Segregation)
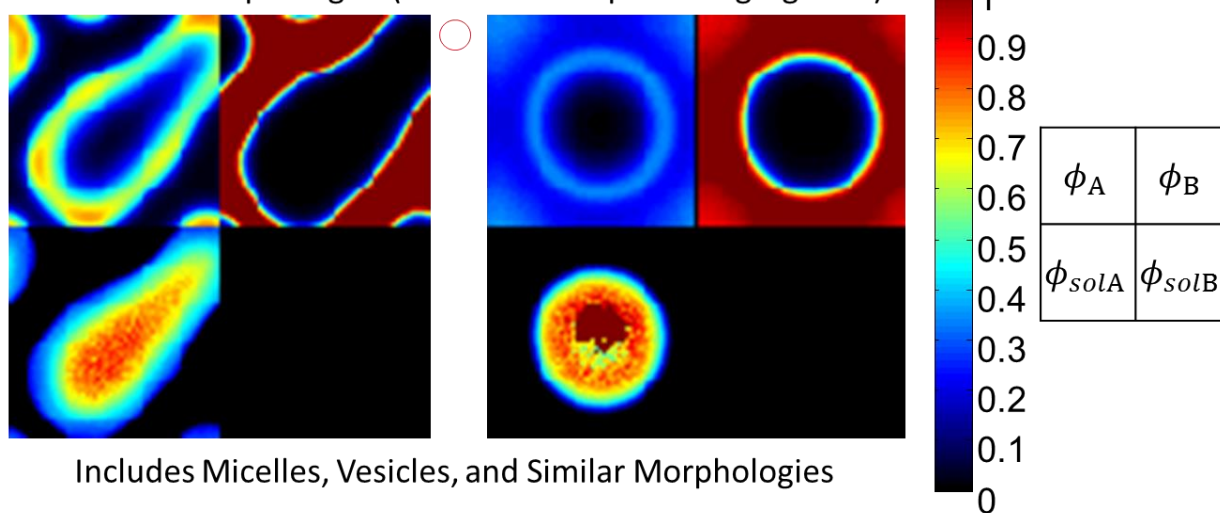
Includes Micelles, Vesicles, and Similar Morphologies

ϕ_A	ϕ_B
ϕ_{solA}	ϕ_{solB}

Figure S15: Examples of two phase morphologies. The solvent density no longer homogenously coincides with the polymer densities. (Left) Simulation conditions are $f = 0.38$ $\chi N = 24$ $\Phi_{sol} = f_{solA} = 0.30$ $f_{eff} = 0.566$. (Right) Simulation conditions are $f = 0.25$ $\chi N = 12$ $\Phi_{sol} = f_{solA} = 0.25$ $f_{eff} = 0.4375$.
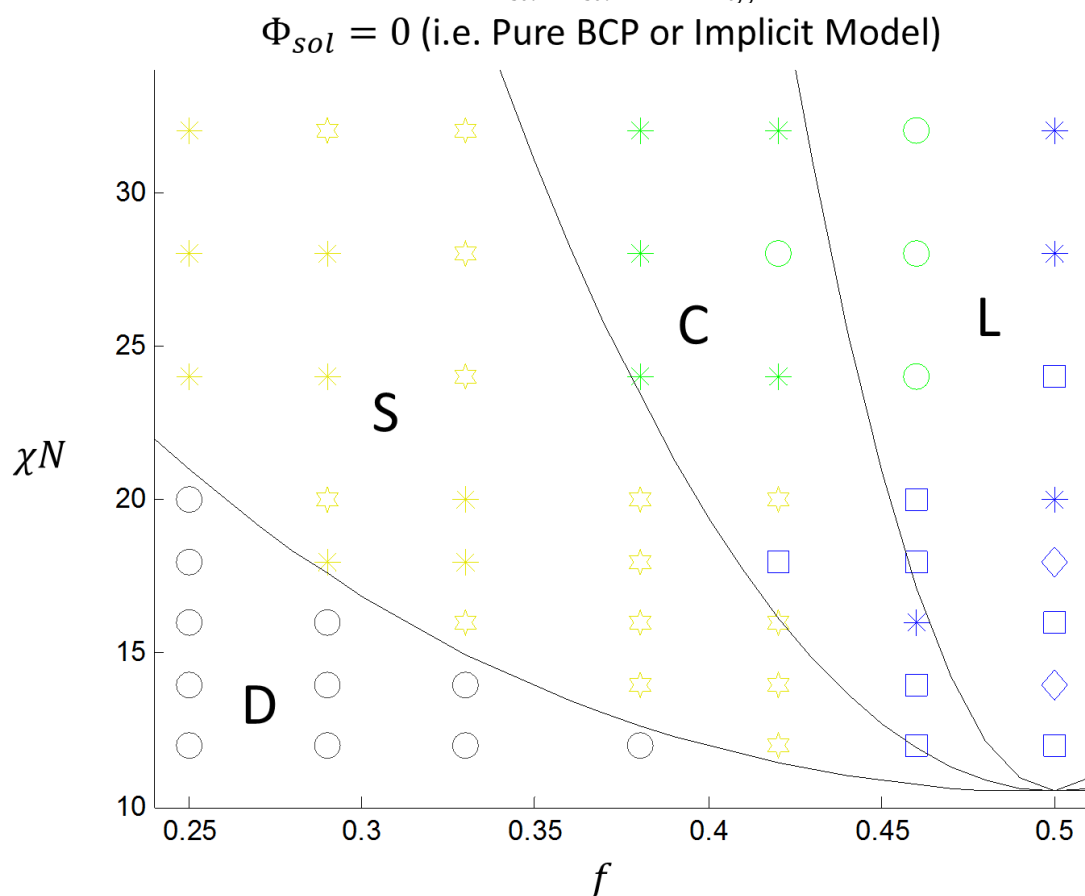

$\Phi_{sol} = 0$ (i.e. Pure BCP or Implicit Model)

Figure S16: Phase diagram for 2D implicit model (aka standard BCP model where χ and f are replaced with their effective values (i.e. $\chi = \chi_{eff}$ and $f = f_{eff}$). Symbols correspond to the symbols above observed phases in Figures S12 through S15. Lines show approximate boundaries for the standard BCP phase diagram phases of lamellae, cylinders, spheres, and disorder (other phases such as gyroid are omitted since only 2D morphologies were examined).
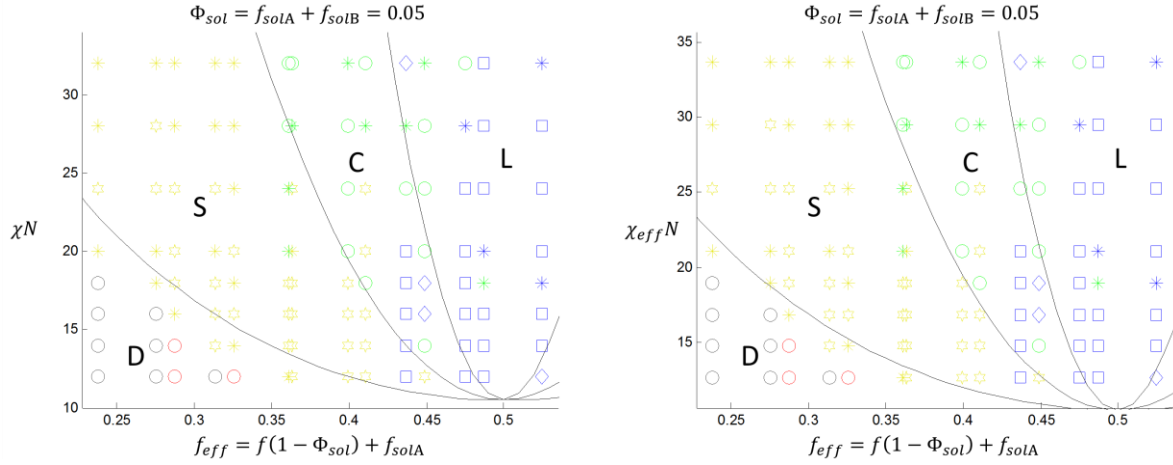
Figure S17: Phase diagrams for explicit solvent model with $\Phi_{sol} = 0.05$. (Left) χN as input into simulation. (Right) $\chi_{eff} = \chi(1 - \Phi_{sol})^{-1}$ replaces χ.

Figure S18: Phase diagrams for explicit solvent model with $\Phi_{sol} = 0.10$. (Left) χN as input into simulation. (Right) $\chi_{eff} = \chi(1 - \Phi_{sol})^{-1}$ replaces χ.
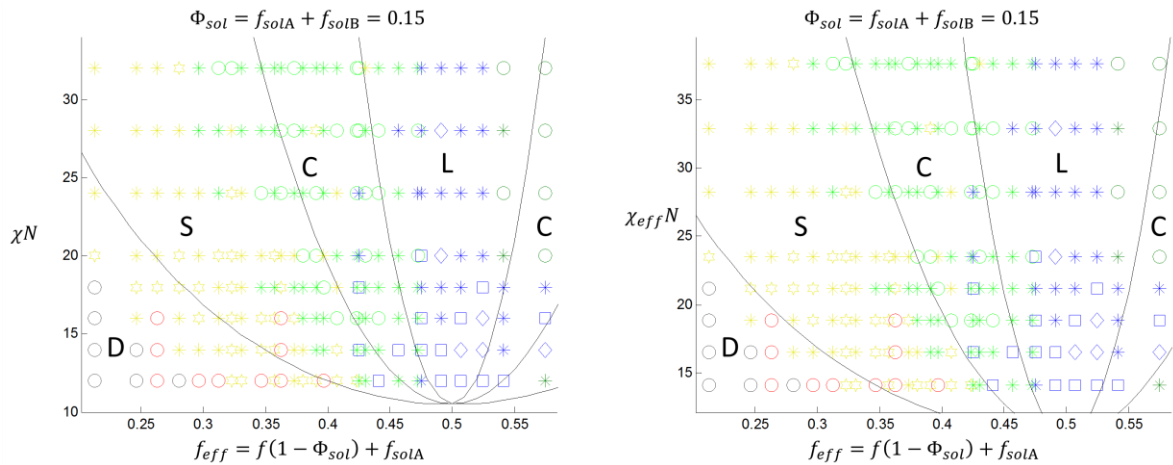
Figure S19: Phase diagrams for explicit solvent model with $\Phi_{sol} = 0.15$. (Left) χN as input into simulation. (Right) $\chi_{eff} = \chi(1 - \Phi_{sol})^{-1}$ replaces χ.

Figure S20: Phase diagrams for explicit solvent model with $\Phi_{sol} = 0.20$. (Left) χN as input into simulation. (Right) $\chi_{eff} = \chi(1 - \Phi_{sol})^{-1}$ replaces χ.
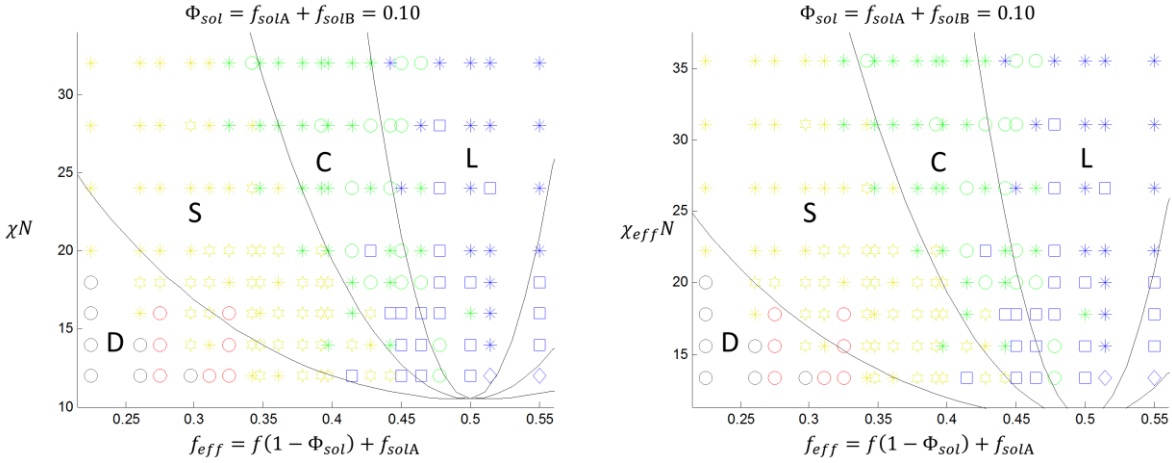

Figure S21: Phase diagrams for explicit solvent model with $\Phi_{sol} = 0.25$. (Left) χN as input into simulation. (Right) $\chi_{eff} = \chi(1 - \Phi_{sol})^{-1}$ replaces χ.

Figure S22: Phase diagrams for explicit solvent model with $\Phi_{sol} = 0.30$. (Left) χN as input into simulation. (Right) $\chi_{eff} = \chi(1 - \Phi_{sol})^{-1}$ replaces χ.
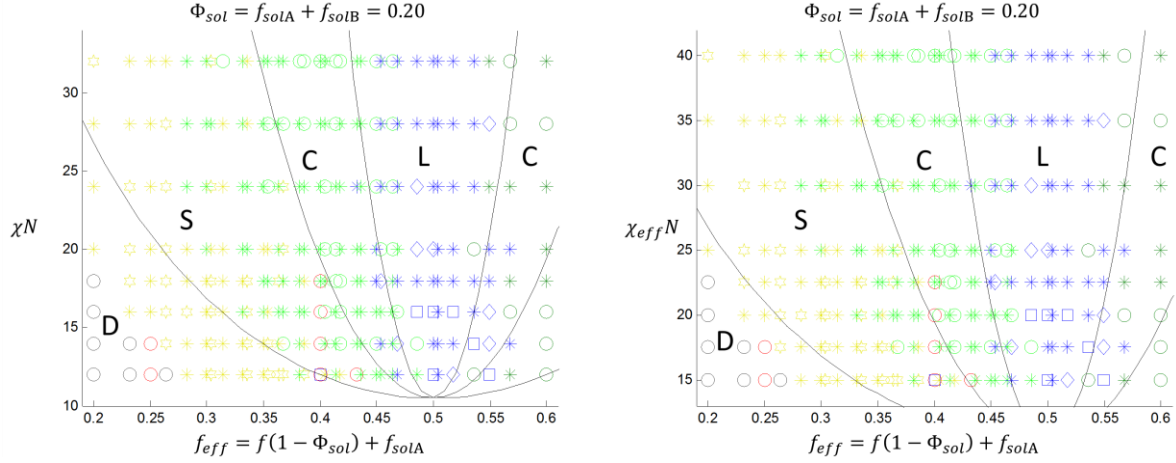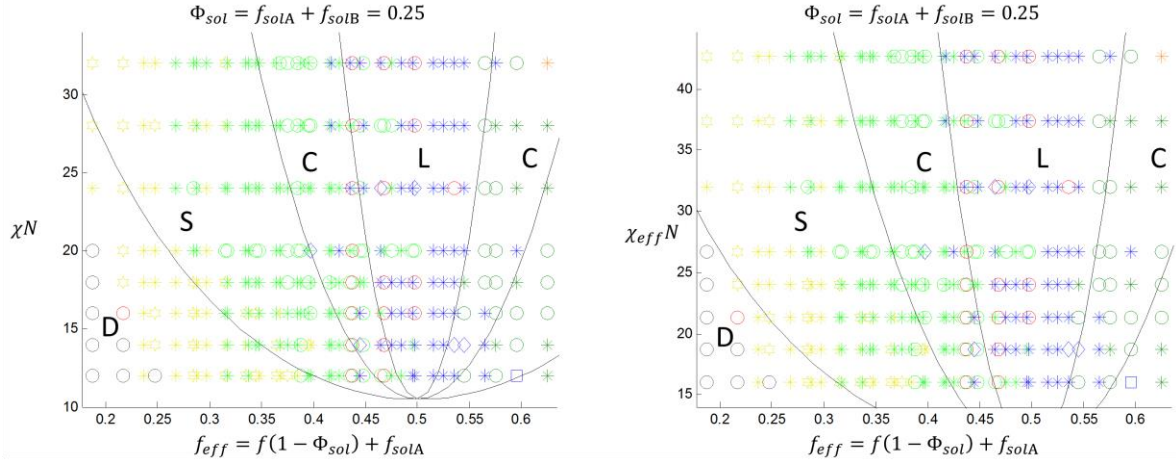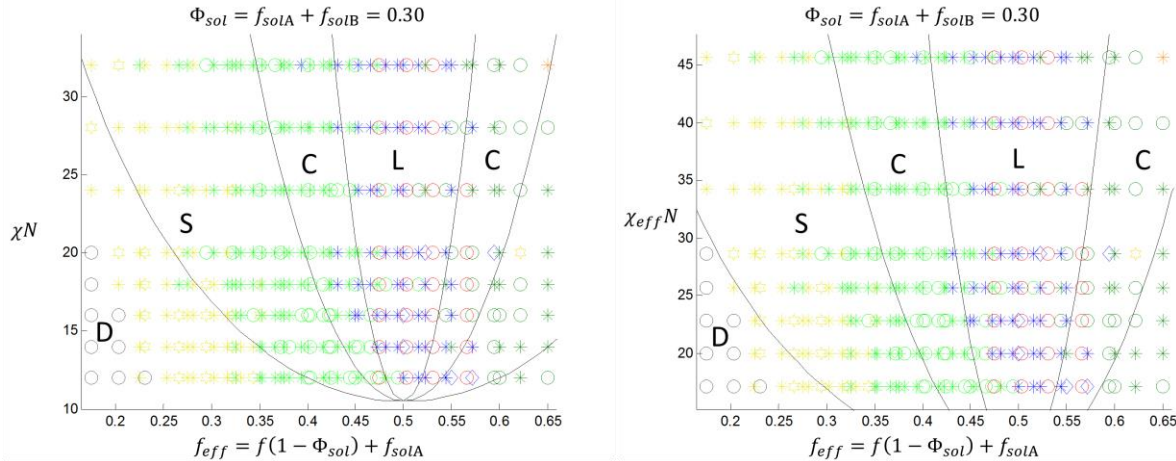
For cases where macrophase segregation does not occur, it is expected a mapping of the morphologies observed with effective parameters can in principle be done, but the parameter α

24

relating χ_{eff} to the input χ will in principle be a function of the ratio of the selective solvents f_{solA} to f_{solB} as will be demonstrated in the following section, describing the dependency of L_0 on the solvent incorporated. Where in the preceding phase diagrams $\alpha = -1$ was assumed, the actual value will vary with both selectivity and amount of solvent incorporated into the system. In fact, the simple model $\chi_{eff} = \chi(1 - \Phi_{sol})^{\alpha}$ appears to break down at high solvent fraction depending on the ratio of selective solvent fractions. For the experimental system of PS-PDMS in toluene and heptane, only heptane is nearly fully selective to one of the blocks, implying the explicit model presented here is inadequate to fully model the system due to the neutral selectivity of toluene mitigating interfacial interactions (i.e. reducing χ_{eff} with added solvent). From these additional simulations, the observation is made that purely selective solvents only increase χ_{eff} (under the assumption of $\chi_{eff} = \chi(1 - \Phi_{sol})^{\alpha}$) due to the solvents swelling the regions inside the corresponding block.

S9: 1D Study of Explicit Model with Natural Periodicity

To understand better how L_0 is affected by solvent uptake, explicit model simulations were performed in 1D over a range of χN with $f = 0.5$ and two ranges of Φ_{sol}. For one range, Φ_{sol} was varied as $f_{solA} = 0.02$ in steps of 0.02 up to 0.50; for the other range, Φ_{sol} was varied as $f_{solA} = f_{solB} = 0.01$ in steps of 0.01 up to 0.25 such that the total solvent fraction Φ_{sol} varied from 0.02 up to 0.50. These two cases covered the two extreme possibilities of fully selective solvents (the first case being only having one selective solvent preferential to one block and the other case equal amounts preferential to both blocks). Unit cell calculations were performed with the length of the box L varied around the expected L_0 based on the strong segregation relationship $L_0 \cong \lambda \chi^{1/6} N^{2/3}$. From these simulation results, density profiles were extracted corresponding to the first period minimum in free energy with respect to period spacing. Example density profiles for all species present are shown in Figure S23 for the equal A and B mix case and Figure S24 for the A solvent only case.
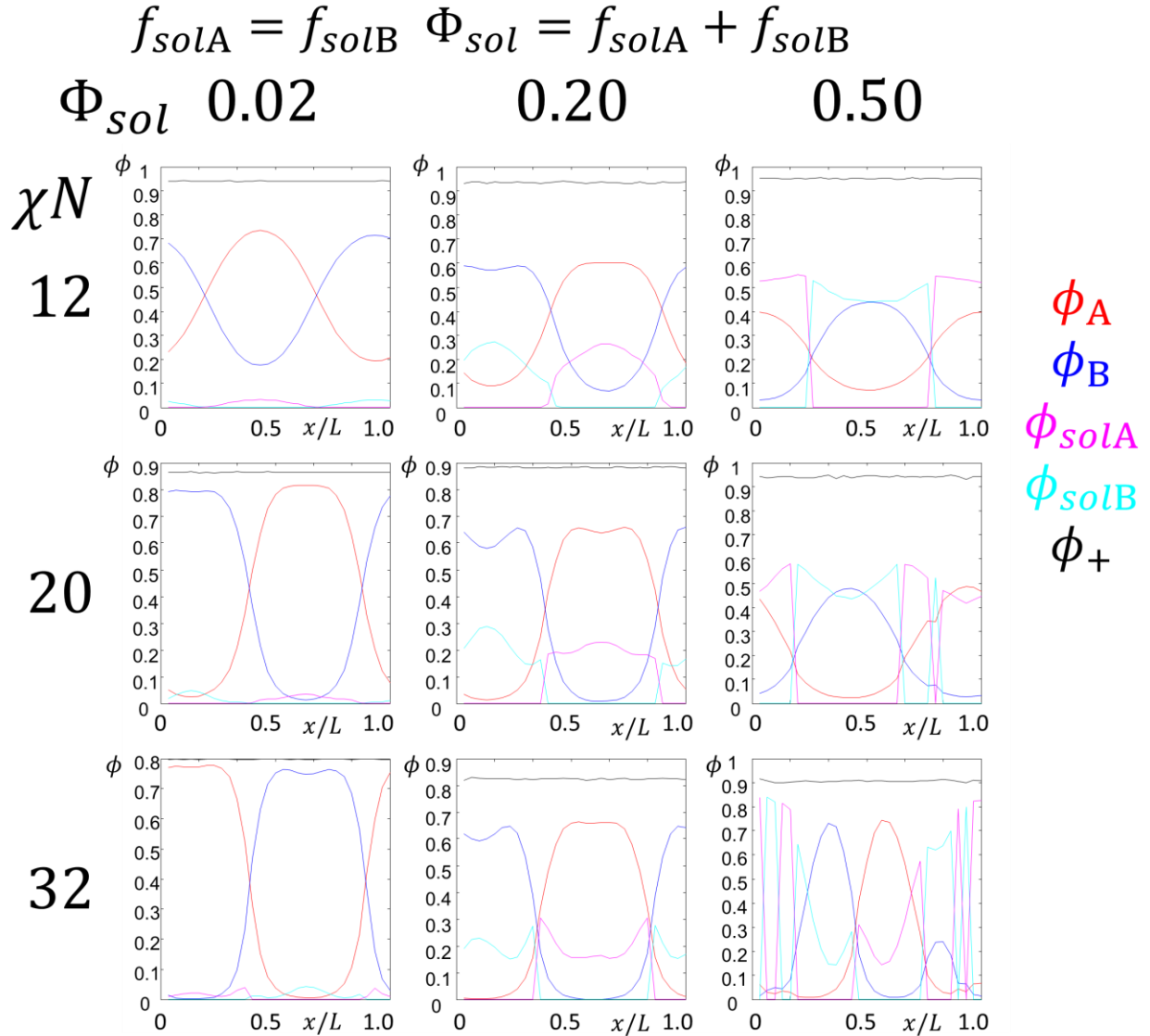
$$f_{sol\text{A}} = f_{sol\text{B}} \quad \Phi_{sol} = f_{sol\text{A}} + f_{sol\text{B}}$$

Figure S23: 1D ϕ density plots of normalized species densities as a function of normalized simulation cell position x/L in the explicit solvent model for representative χN and Φ_{sol}. Here $f_{sol\text{A}} = f_{sol\text{B}}$ with $\Phi_{sol} = f_{sol\text{A}} + f_{sol\text{B}}$. Densities are colour coded with red for the A polymer block ϕ_A, blue for the B polymer block ϕ_B, magenta for the A solvent $\phi_{sol\text{A}}$, and cyan for the B solvent $\phi_{sol\text{B}}$. The total density $\phi_+ = \phi_\text{A} + \phi_\text{B} + \phi_{sol\text{A}} + \phi_{sol\text{B}}$ is colour coded black and should be very close to 1 with some deviations due to numerical integration error as well as higher χN causing the equilibrated chains to be slightly compressed.

For the A and B equal mix case with Φ_{sol} close to 0, the polymer densities resemble the profiles of pure BCP with some perturbation at the center of the of the polymer domain. For moderate concentrations (e.g. $\Phi_{sol} = 0.20$) this perturbation increases and leads to solvent displacing polymer density at the center of the block profiles causing their density curves to flatten or bevel downwards in some cases. Note that the A and B densities look different in some cases, which is due to the fact two different λ values were used such that $\lambda_\text{A}/\lambda_\text{B} = 1.2$ as PDMS

26

has a slight larger Kuhn length than PS. For large solvent concentrations, macrophase separation is observed at higher χN values with the block copolymer density profiles being compressed in the cell length direction and the solvent occupying the surrounding space. In these regions, there is great discontinuity in the A solvent and B solvent density profiles which is likely because the mean field theory is not applicable for this solvent range. Thus the exact density profiles in these regions should not be taken quantitatively but only qualitatively at best. One other observation is that for high χN, the solvent profile inside the block domains does appear to start mediating BCP surface interactions, because the solvent profiles increase from the center of the domain until a sudden drop at the interface. A neutral solvent would be expected to behave similarly but without the drop off, rather decreasing toward the center of the other domain. This suggests the model may be qualitatively adequate for modeling neutral-like solvents in the high χN, moderate Φ_{sol} regime, if the identity of the solvent is ignored.

For the case of only A solvent with Φ_{sol} close to 0, the polymer densities again resemble the profiles of pure BCP with some perturbation at the center of the of the A polymer domain. For moderate concentrations (e.g. $\Phi_{sol} = 0.20$) this perturbation now leads to the A domain becoming bimodal with the solvent occupying the center area. For large A solvent concentrations, the A density becomes spread out over a very large region suggesting the formation of some kind of micellar structure. The B domains at these high Φ_{sol} values are compressed into a small region which would indicate something similar to the formation of micelles with a B center surrounded by A solvent.
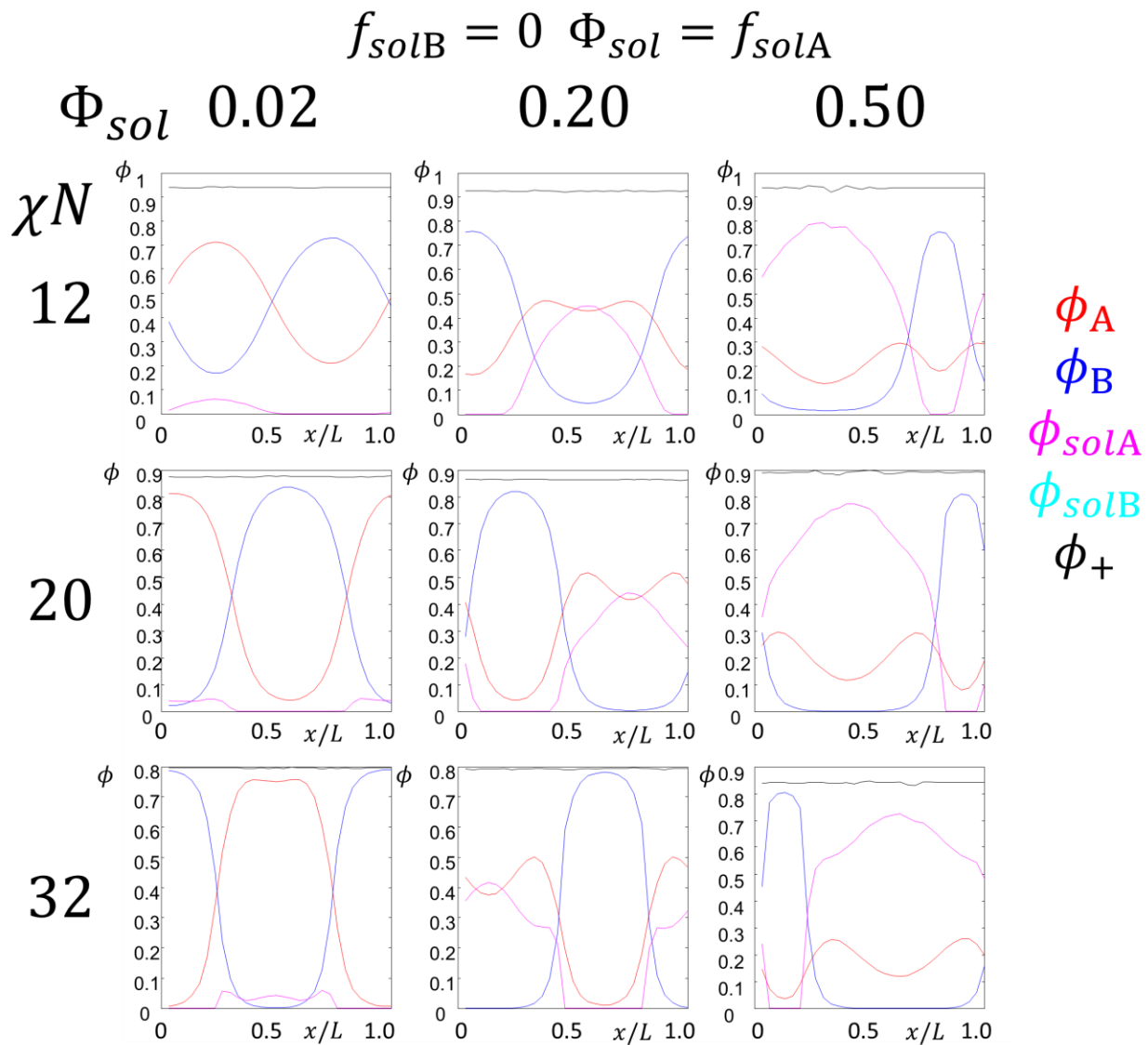
Figure S24: 1D density plots of normalized species densities as a function of normalized simulation cell position x/L in the explicit solvent model for representative χN and Φ_{sol}. Here $f_{solB} = 0$ with $\Phi_{sol} = f_{solA}$. Densities are colour coded with red for the A polymer block ϕ_A, blue for the B polymer block ϕ_B, magenta for the A solvent ϕ_{solA}, and cyan for the B solvent ϕ_{solB}. The total density $\phi_+ = \phi_A + \phi_B + \phi_{solA} + \phi_{solB}$ is colour coded black and should be very close to 1 with some deviations due to numerical integration error as well as higher χN causing the equilibrate chains to be slightly compressed.

Having obtained these profiles corresponding to roughly one natural period of a 3D equivalent lamellar morphology (in 1D of course just being represented by sinusoidal-like density profiles), free energy calculations for the morphology were performed by holding those density fields constant and calculating the corresponding chemical potential fields necessary for those profiles to satisfy the SCFT saddle point equations. This produced free energy curves with respect to the unit cell length L that were then fit with the relationship

$$F(L) = \Gamma L^2 + \frac{\sigma}{L} - \epsilon \quad \text{(ES16)}$$

which is the normal form of the strain energy contribution to the free energy (which should be the dominant energy term for the strained unit cells). L_0 for a given solvent incorporation amount was then determined as the L corresponding to the minimum of these curves,

$$L_0 = (\sigma/2\Gamma)^{1/3} . \quad \text{(ES17)}$$

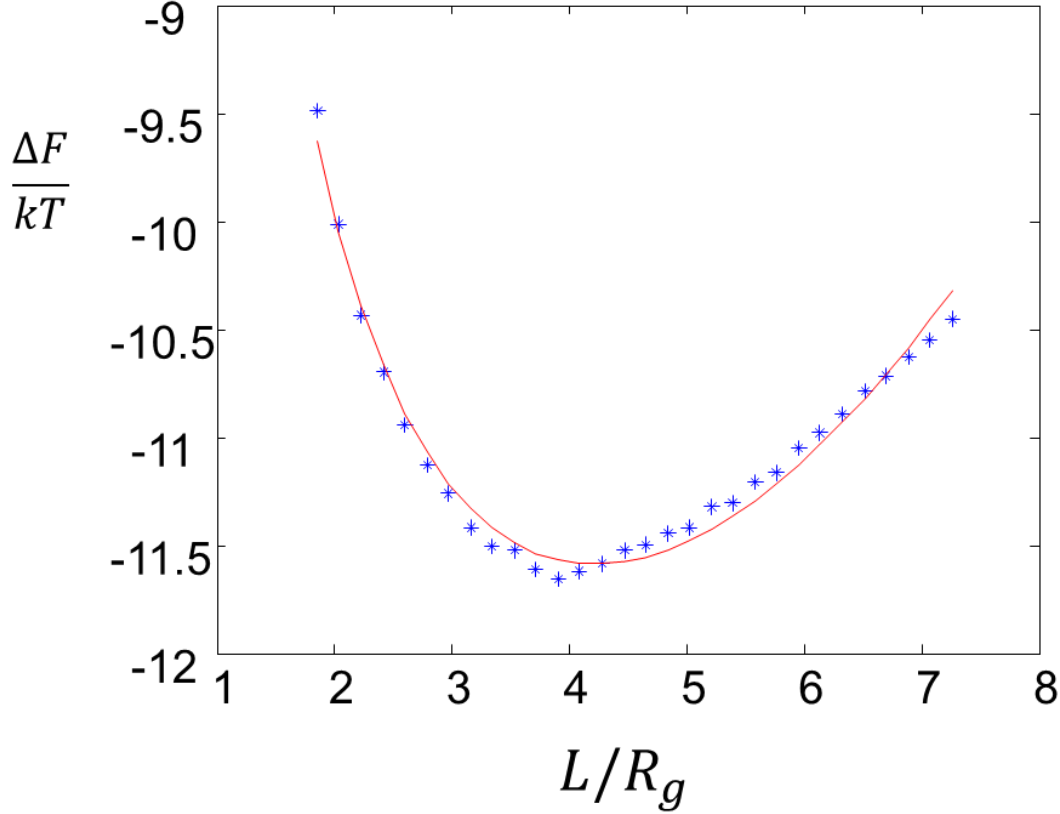Figure S25 shows a representative curve with data and fit.

Figure S25: Representative free energy plot (normalized to kT and shifted such that the ODT energy is 0 (negative energy is ordered microphase separated, positive is disordered) plotted versus the normalized unit cell length to the radius of gyration R_g for an $N = 125$ chain. Blue stars are the calculated energy values for fixed ϕ_- and ϕ_+ and red curve is the fit with form $F(L) = \Gamma L^2 + \sigma/L - \epsilon$.

Having obtained these values for L_0 as a function of f_{solA} and f_{solB} over a range of χN for $f = 0.5$, fits were found for L_0 as a function of χ, N, and Φ_{sol} with two functional forms. The first functional form

$$L_0 \cong \lambda \chi^{\delta_0} N^{\beta_0} (1 - \Phi_{sol})^\gamma \quad \text{(ES18)}$$

was found by first finding a best fit for δ_0 and β_0 from simulations with $\Phi_{sol} = 0$. This fit is shown in Figure S26 for the implicit solvent or standard BCP model case ($\Phi_{sol} = 0$).

$$\gamma(\Phi_{sol}) = -\alpha(\Phi_{sol})\delta_0 \quad (ES19)$$

was found by fitting each constant value of Φ_{sol}. The strong segregation limit is known to have $\delta_0 = 1/6$ and $\beta_0 = 2/3$, and here in the weak segregation regime values slightly less than those values were found for the implicit or standard BCP case ($\Phi_{sol} = 0$)[13].
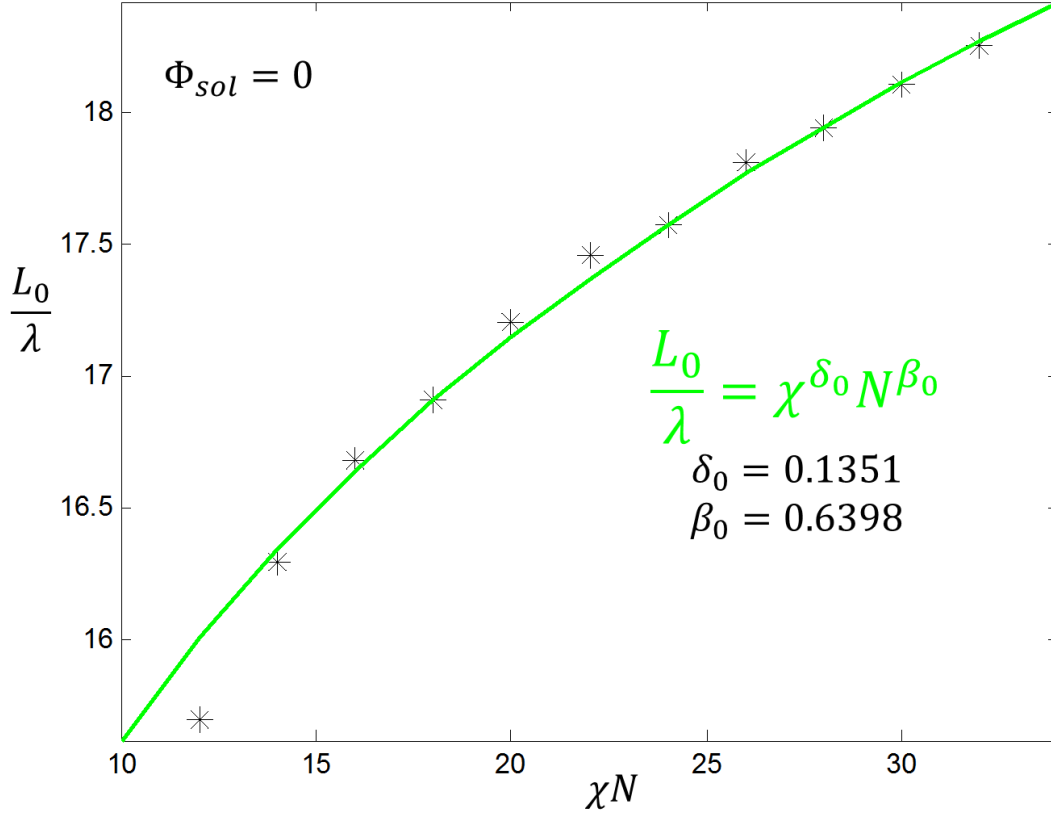

Figure S26: Plot of normalized L_0 by Kuhn segment length λ versus χN for $\Phi_{sol} = 0$ (standard BCP system or implicit model with $\chi \to \chi_{eff}$ and $f \to f_{eff}$ for $f = 0.50$. χN is in the weak segregation regime, so $\delta_0 < 1/6$ and $\beta_0 < 2/3$ but very close to those values as expected from previous work[13]. The green line is the best fit to the simulated data and the black stars the calculated L_0 values.

The second functional form assumes that the exponents $\delta = \delta(\Phi_{sol})$ and $\beta = \beta(\Phi_{sol})$ and thus accounts for the effective increase in χ from the selective solvents implicitly such that

$$L_0 = \lambda\chi^{\delta(\Phi_{sol})}N^{\beta(\Phi_{sol})}. \quad (ES20)$$

Results of both fits for different χN and Φ_{sol} for both the A only selective solvent case and the A and B mixture case are shown in Figures S27 through S30 plotted versus both χN for constant Φ_{sol} and against Φ_{sol} for constant χN. For the A and B mixture case, both fits matched the data relatively well with the second model varying δ and β with Φ_{sol} having slightly better fits. The

first model with α works better for higher χN in general. For the A only solvent, the first model with α appears to break down for $\Phi_{sol} > \sim 0.20$ with goodness of fits values rapidly increasing with increasing Φ_{sol}, whereas the second model fits the data well for most of the data range. In this case, the first model fits best in the intermediate χN regime and has a very poor goodness of fit for low and high χN. This suggests that the values extracted for α for the A only solvent systems should not be taken as completely accurate but rather as general trends on how the exponent varies. Additionally, the second model is just a mathematical fit to the data using the standard scaling form of the natural period with the assumption δ and β are a function of Φ_{sol} which may not be entirely true (i.e. just because allowing those parameters to vary produces a good fit to the data, the values obtained from their fits are empirical at best).
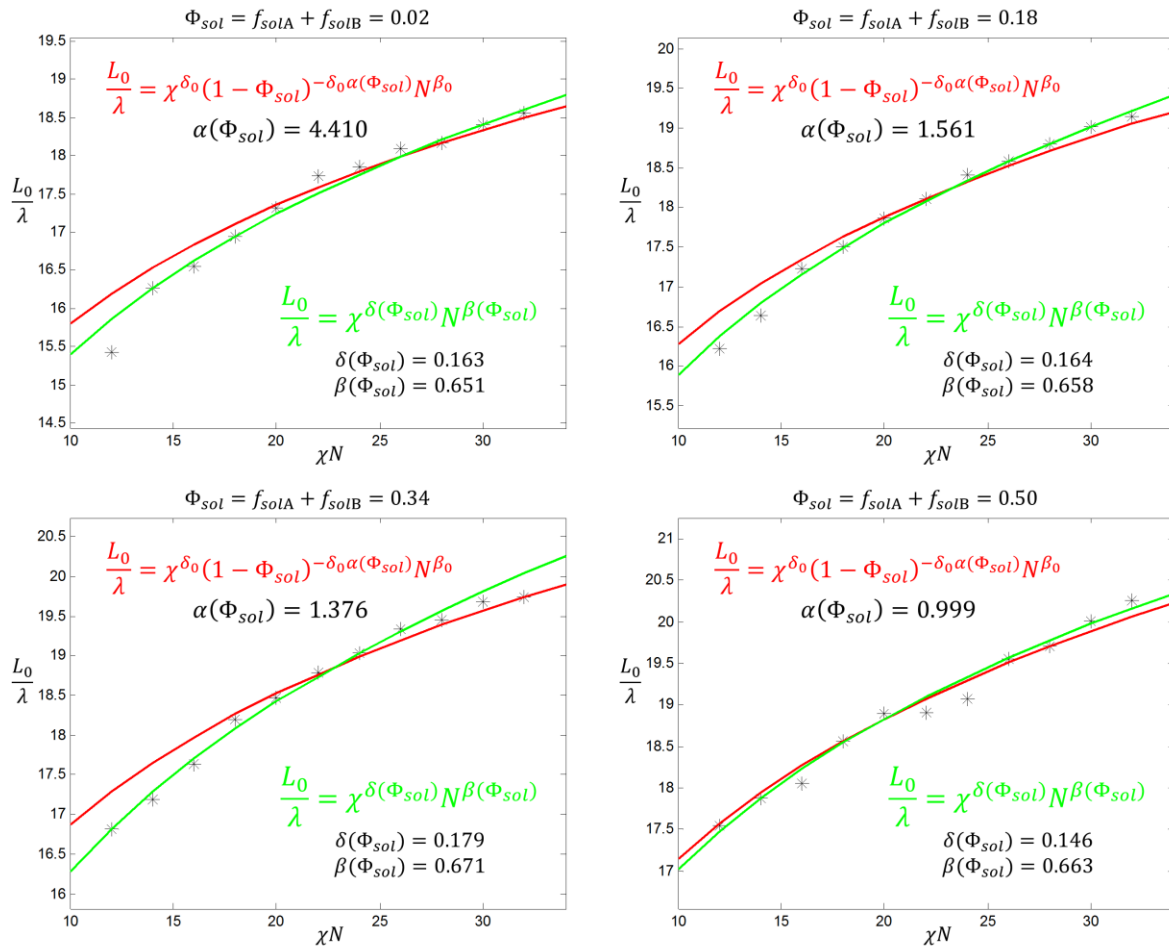
Figure S27: Plot of normalized L_0 by Kuhn segment length λ versus χN for A and B equal solvent mix with $\Phi_{sol} = 0.02, 0.18, 0.34,$ and 0.50 and $f = 0.50$. The black stars are the calculated L_0 values. The red lines are the best fit to the simulated data using the model equation $L_0/\lambda = \chi^{\delta_0}(1 - \Phi_{sol})^{-\delta_0\alpha(\Phi_{sol})}N^{\beta_0}$, where δ_0 and β_0 are the $\Phi_{sol} = 0$ fit parameters for L_0/λ as a function of χ and N. The green lines use the model equation $L/\lambda = \chi^{\delta(\Phi_{sol})}N^{\beta(\Phi_{sol})}$.
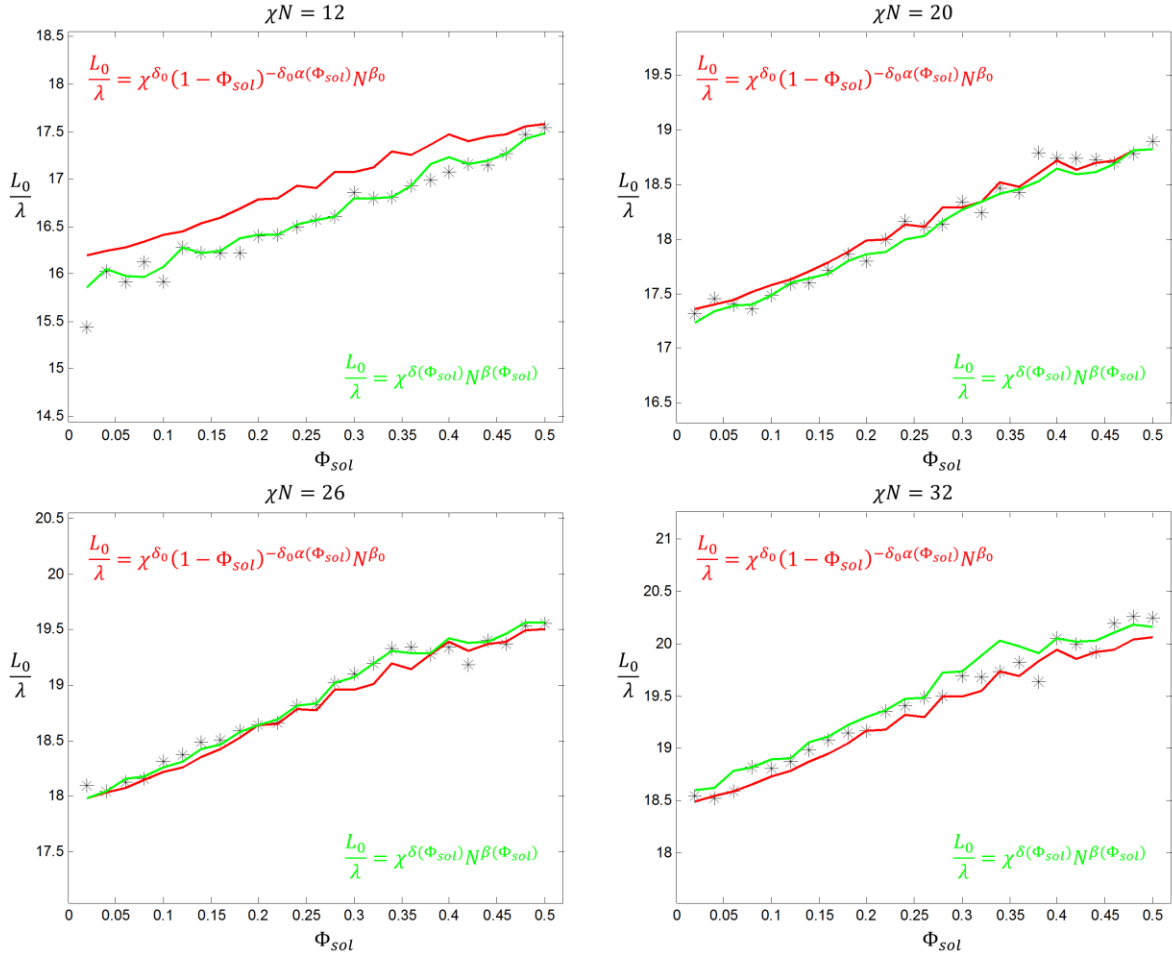
Figure S28: Plot of normalized L_0 by Kuhn segment length λ versus Φ_{sol} for A and B equal solvent mix with $\chi N = 12, 20, 26,$ and 32 and $f = 0.50$. The black stars are the calculated L_0 values. The red lines are the best fit to the simulated data using the model equation $L_0/\lambda = \chi^{\delta_0}(1 - \Phi_{sol})^{-\delta_0 \alpha(\Phi_{sol})} N^{\beta_0}$, where δ_0 and β_0 are the $\Phi_{sol} = 0$ fit parameters for L_0/λ as a function of χ and N. The green lines use the model equation $L/\lambda = \chi^{\delta(\Phi_{sol})} N^{\beta(\Phi_{sol})}$.

$\Phi_{sol} = f_{solA} = 0.02$

$$\frac{L_0}{\lambda} = \chi^{\delta_0}(1 - \Phi_{sol})^{-\delta_0 \alpha(\Phi_{sol})} N^{\beta_0}$$

$$\alpha(\Phi_{sol}) = 3.563$$

$$\frac{L_0}{\lambda} = \chi^{\delta(\Phi_{sol})} N^{\beta(\Phi_{sol})}$$

$$\delta(\Phi_{sol}) = 0.150$$
$$\beta(\Phi_{sol}) = 0.647$$

$\Phi_{sol} = f_{solA} = 0.18$

$$\frac{L_0}{\lambda} = \chi^{\delta_0}(1 - \Phi_{sol})^{-\delta_0 \alpha(\Phi_{sol})} N^{\beta_0}$$

$$\alpha(\Phi_{sol}) = 1.847$$

$$\frac{L_0}{\lambda} = \chi^{\delta(\Phi_{sol})} N^{\beta(\Phi_{sol})}$$

$$\delta(\Phi_{sol}) = 0.187$$
$$\beta(\Phi_{sol}) = 0.669$$

$\Phi_{sol} = f_{solA} = 0.34$

$$\frac{L_0}{\lambda} = \chi^{\delta_0}(1 - \Phi_{sol})^{-\delta_0 \alpha(\Phi_{sol})} N^{\beta_0}$$

$$\alpha(\Phi_{sol}) = 2.831$$

$$\frac{L_0}{\lambda} = \chi^{\delta(\Phi_{sol})} N^{\beta(\Phi_{sol})}$$

$$\delta(\Phi_{sol}) = 0.253$$
$$\beta(\Phi_{sol}) = 0.713$$

$\Phi_{sol} = f_{solA} = 0.50$

$$\frac{L_0}{\lambda} = \chi^{\delta_0}(1 - \Phi_{sol})^{-\delta_0 \alpha(\Phi_{sol})} N^{\beta_0}$$

$$\alpha(\Phi_{sol}) = 3.529$$

$$\frac{L_0}{\lambda} = \chi^{\delta(\Phi_{sol})} N^{\beta(\Phi_{sol})}$$

$$\delta(\Phi_{sol}) = 0.451$$
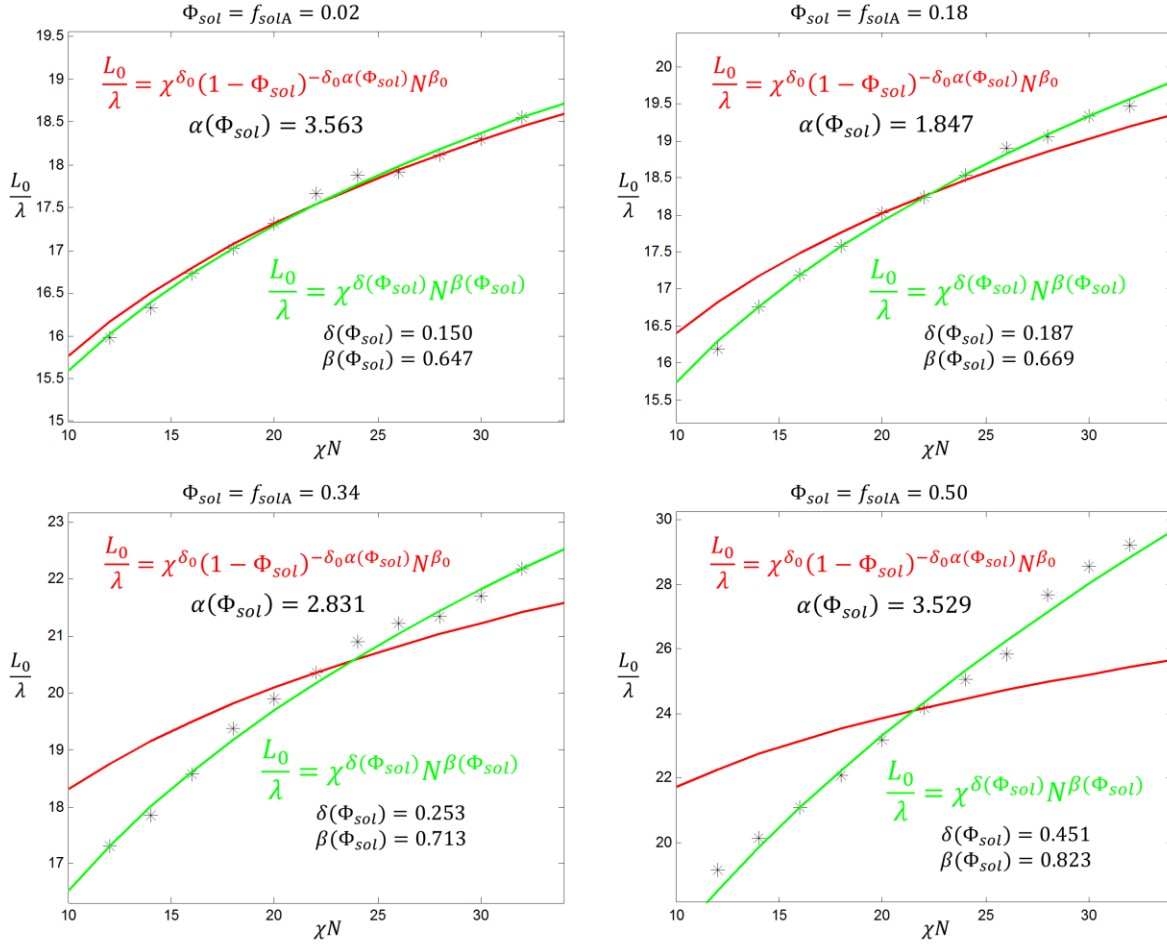$$\beta(\Phi_{sol}) = 0.823$$

Figure S29: Plot of normalized L_0 by Kuhn segment length λ versus χN for A solvent only with $\Phi_{sol} = 0.02, 0.18, 0.34,$ and 0.50 and $f = 0.50$. The black stars are the calculated L_0 values. The red lines are the best fit to the simulated data using the model equation $L_0/\lambda = \chi^{\delta_0}(1 - \Phi_{sol})^{-\delta_0 \alpha(\Phi_{sol})} N^{\beta_0}$, where δ_0 and β_0 are the $\Phi_{sol} = 0$ fit parameters for L_0/λ as a function of χ and N. The green lines use the model equation $L/\lambda = \chi^{\delta(\Phi_{sol})} N^{\beta(\Phi_{sol})}$.
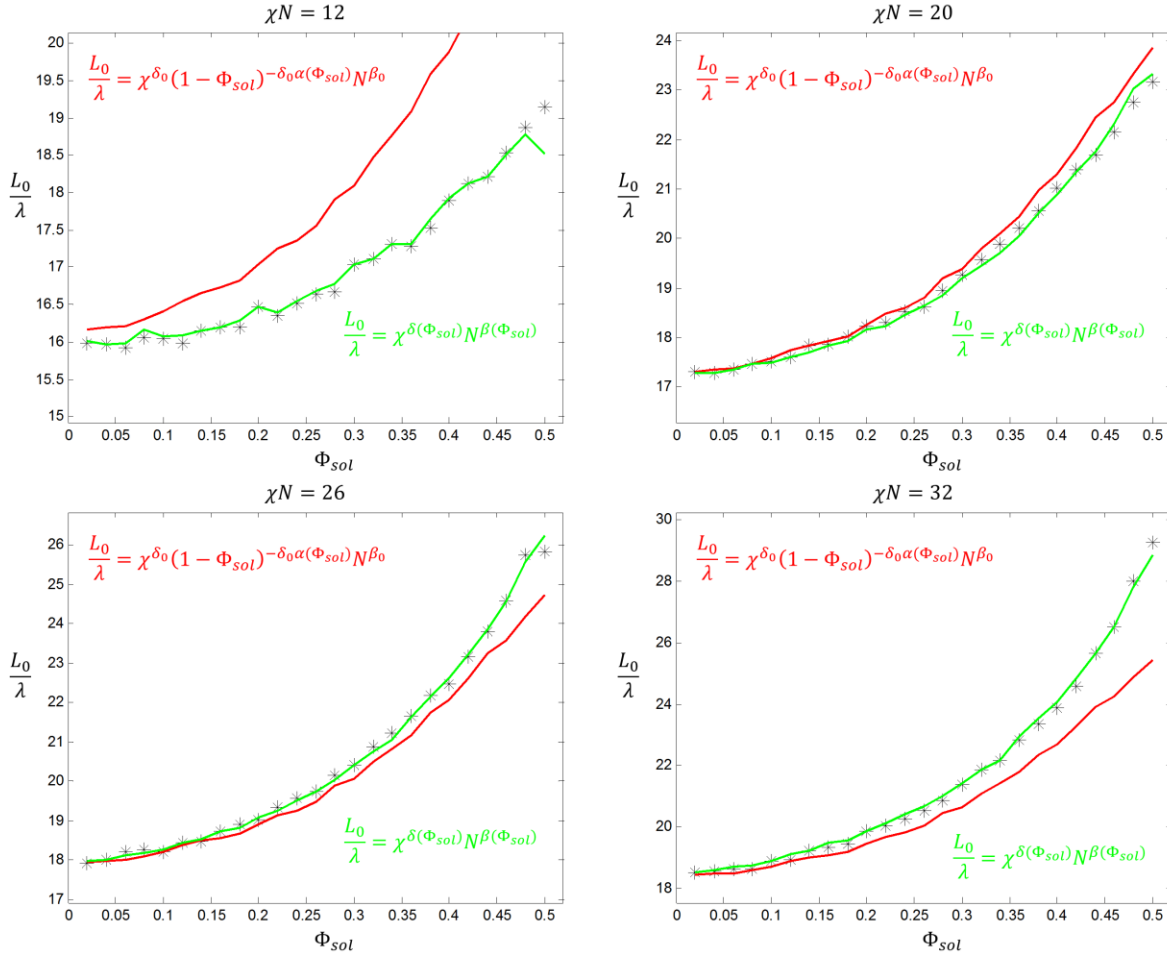
Figure S30: Plot of normalized L_0 by Kuhn segment length λ versus Φ_{sol} for A solvent only with $\chi N = 12, 20, 26,$ and 32 and $f = 0.50$. The black stars are the calculated L_0 values. The red lines are the best fit to the simulated data using the model equation $L_0/\lambda = \chi^{\delta_0}(1 - \Phi_{sol})^{-\delta_0 \alpha(\Phi_{sol})} N^{\beta_0}$, where δ_0 and β_0 are the $\Phi_{sol} = 0$ fit parameters for L_0/λ as a function of χ and N. The green lines use the model equation $L/\lambda = \chi^{\delta(\Phi_{sol})} N^{\beta(\Phi_{sol})}$.

To better characterize the fitting parameters, plots of their values as function of Φ_{sol} are shown in Figures S31 through S34. For the A and B mixture, α decreased with increasing Φ_{sol} for the first model and the parameters δ and β remained relatively constant with values slightly higher than the implicit model or standard BCP results for the second model. For the A solvent only case, α decreased initially then gradually increased with Φ_{sol} for the first model whereas δ and β increased rapidly with increasing Φ_{sol} for the second model.

$$\frac{L_0}{\lambda} = \chi^{\delta_0}(1 - \Phi_{sol})^{-\delta_0 \alpha(\Phi_{sol})} N^{\beta_0}$$
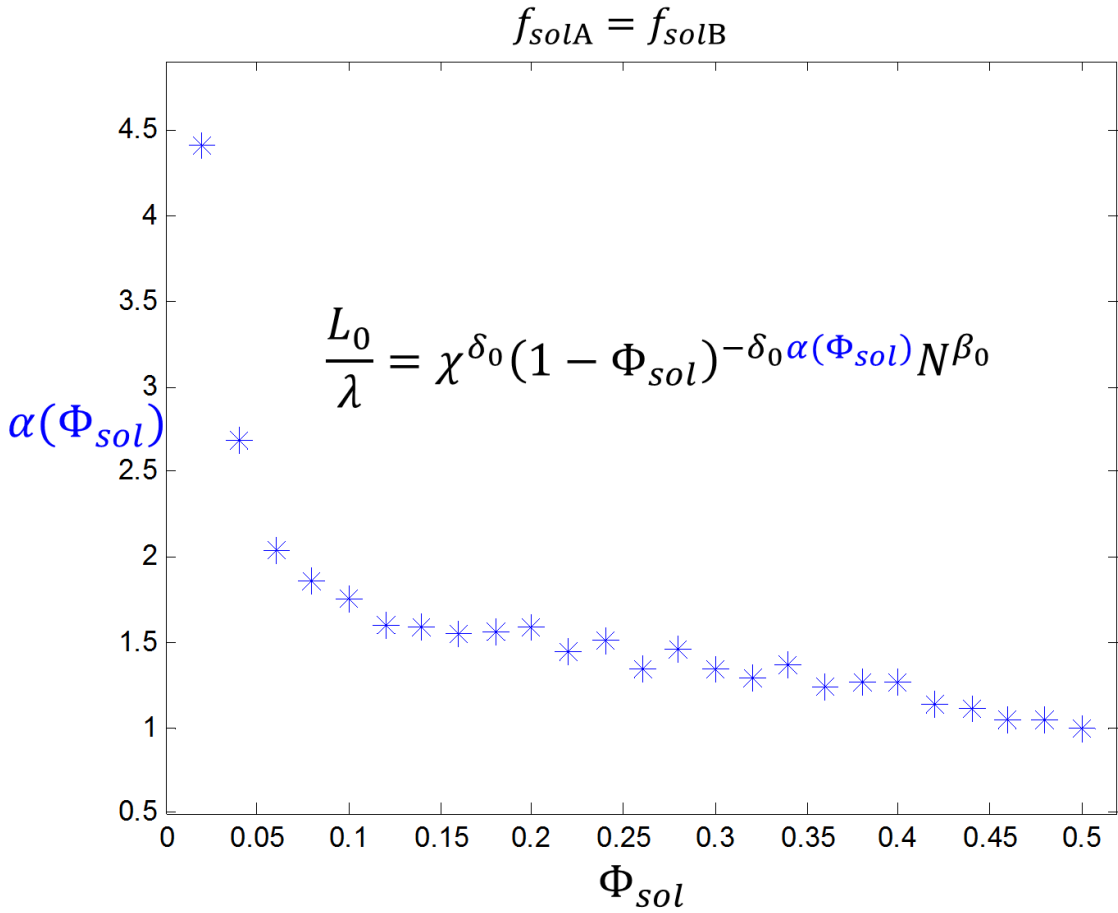
Figure S31: Plot of fit parameter α as a function of solvent fraction Φ_{sol} for the case that both A and B selective solvent is incorporated into the system ($f_{solA} = f_{solB}$ such that $\Phi_{sol} = f_{solA} + f_{solB}$). For low Φ_{sol}, α starts out large, decreases rapidly, and then gradually decreases with increasing Φ_{sol}.
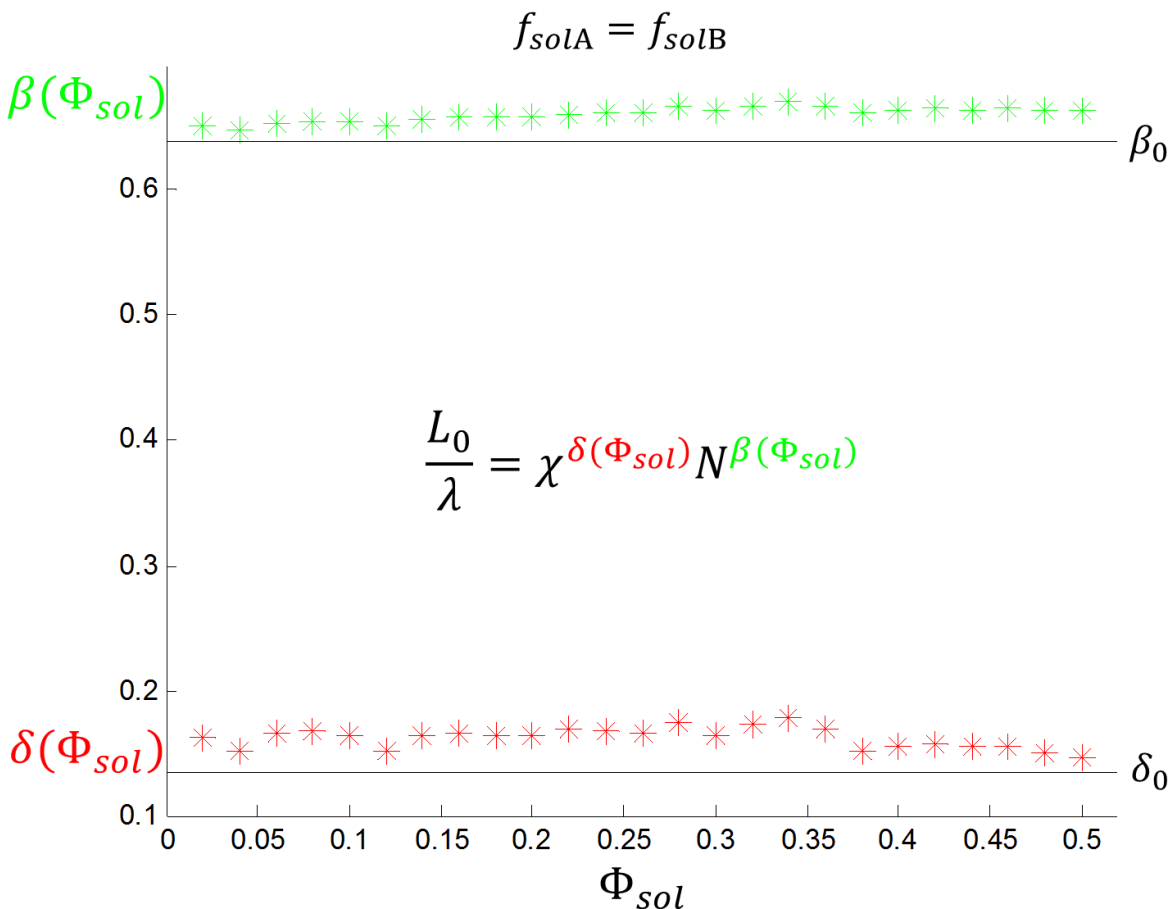
Figure S32: Plot of fit parameters $\delta(\Phi_{sol})$ in red and $\beta(\Phi_{sol})$ in green as a function of solvent fraction Φ_{sol} for the case that both A and B selective solvents are incorporated into the system ($f_{solA} = f_{solB}$ with $\Phi_{sol} = f_{solA} + f_{solB}$). In contrast to the A solvent only case, the parameters start out close to their $\Phi_{sol} = 0$ values of δ_0 and β_0 but slightly higher staying relatively close to that value with an average value of $\delta_{avg} = 0.162 \pm 0.008$ and $\beta_{avg} = 0.661 \pm 0.006$ where the error here is the standard deviation.
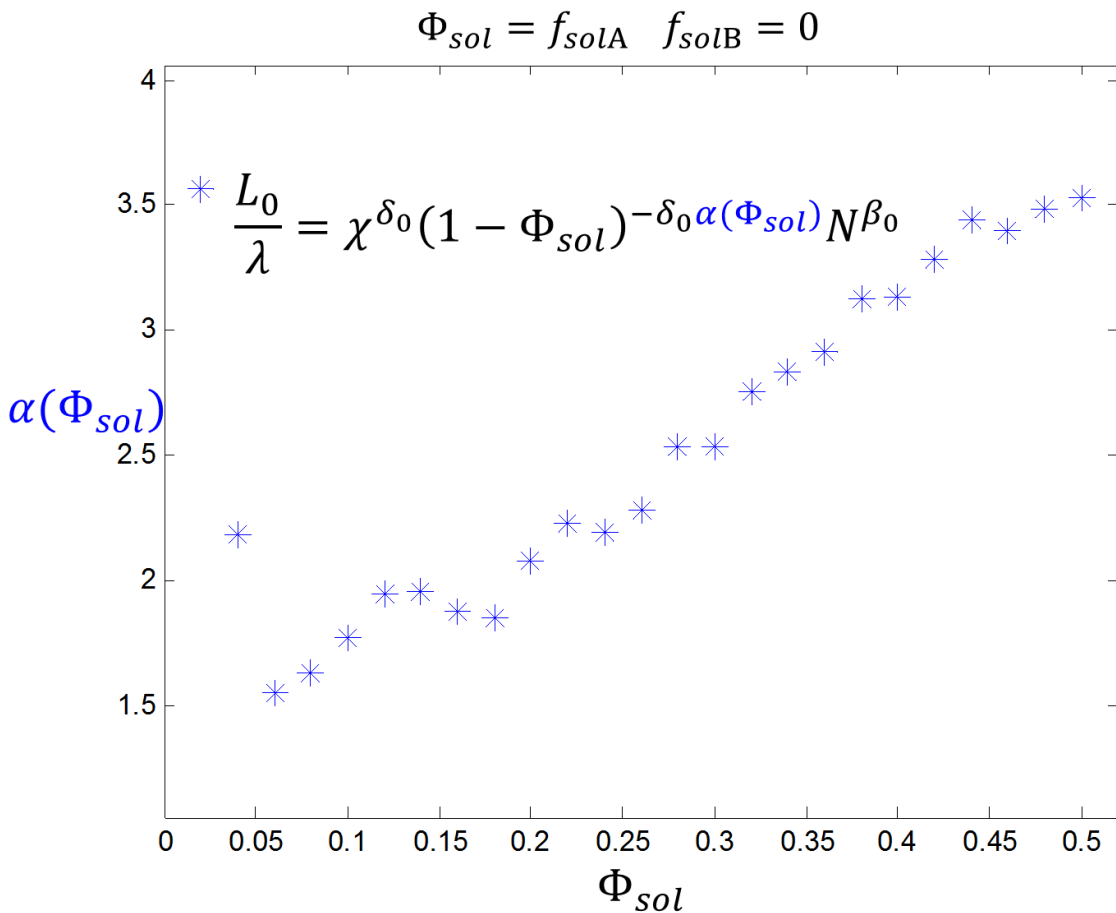
Figure S33: Plot of fit parameter α as a function of solvent fraction Φ_{sol} for the case that only A selective solvent is incorporated into the system ($f_{solB} = 0$ such that $\Phi_{sol} = f_{solA}$). For low Φ_{sol}, α starts out large, decreases rapidly, and then gradually increases with increasing Φ_{sol} in contrast to the equal selective A and B solvent mix where the parameter decreased.
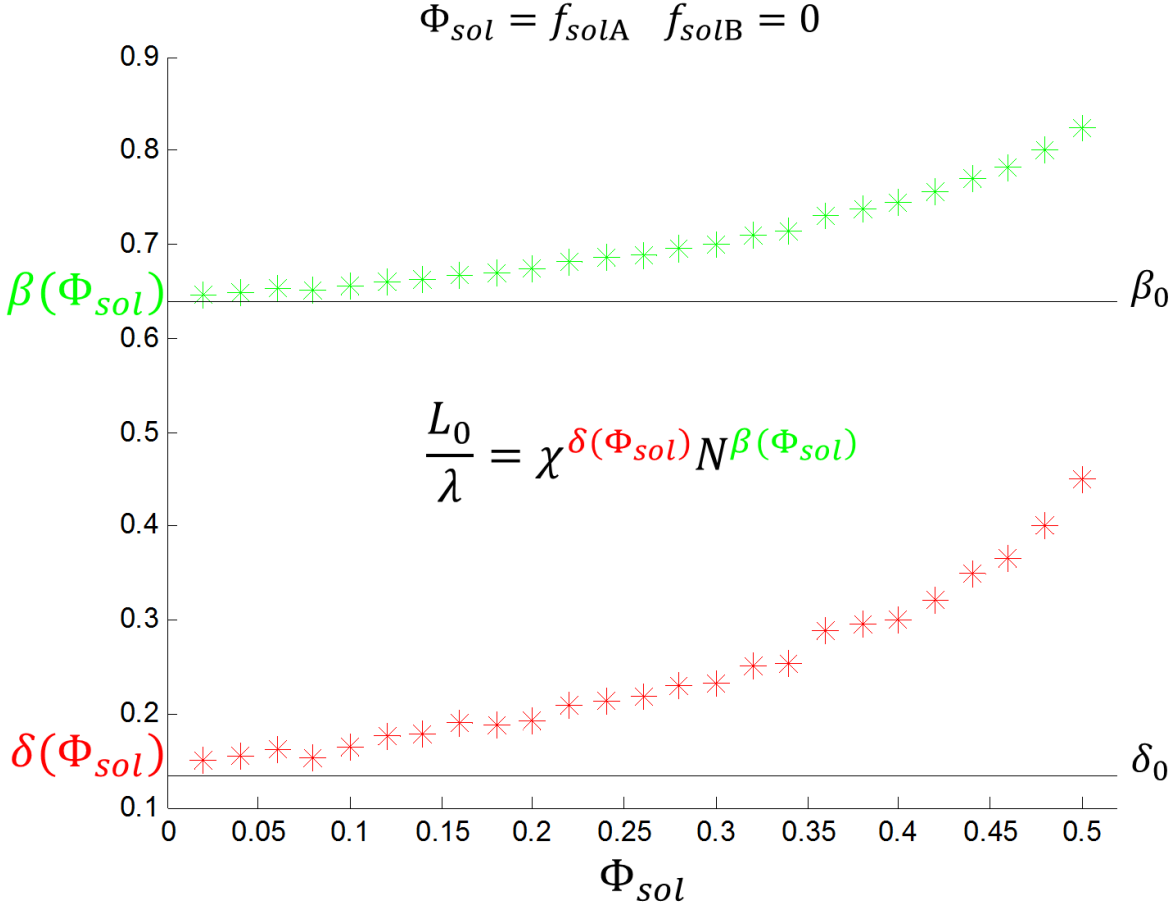
Figure S34: Plot of fit parameters $\delta(\Phi_{sol})$ in red and $\beta(\Phi_{sol})$ in green as a function of solvent fraction Φ_{sol} for the case that only A selective solvent is incorporated into the system ($f_{solB} = 0$ such that $\Phi_{sol} = f_{solA}$). For low Φ_{sol}, the parameters start out close to their $\Phi_{sol} = 0$ values of δ_0 and β_0 (shown as horizontal black lines for reference) and gradually increase to higher values as Φ_{sol} increases.

Using the resulting fit parameters for both solvent selectivity cases and model fits, functional variance of χ_{eff} from each model and solvent combination are deduced. Plots for the first model plotting the ratio of

$$\frac{\chi_{eff}}{\chi} = (1 - \Phi_{sol})^{-\alpha} \quad (ES21)$$

are shown in Figure S35 and for the second model plots of

$$\log \chi_{eff} / \log \chi = \Delta(\Phi_{sol}) = \delta(\Phi_{sol})/\delta_0 \quad (ES22)$$

are shown in Figure S36 and plots of

$$\log N_{eff} / \log N = B(\Phi_{sol}) = \beta(\Phi_{sol})/\beta_0 \quad (ES23)$$

are shown in Figure S37. From these plots, the first model shows that as Φ_{sol} increases, for the A and B mixed case χ_{eff} gradually increases up to a factor of 2 times the normal value at

$\Phi_{sol} = 0.50$ while for the A only solvent case χ_{eff} appears to start increasing almost exponentially with increasing Φ_{sol}. Recalling that this model did not give a great fit to the data for L_0/λ for the A only selective solvent case, this apparent large increase of χ_{eff} should be considered only qualitatively correct. The second model shows different behavior for χ_{eff} depending on if $\chi < 1$ or $\chi > 1$. Since most reported χ values are less than 1 and the ratio $\log \chi_{eff} / \log \chi > 1$ for all $\Phi_{sol} > 0$, this suggests χ_{eff} will be smaller than χ for $\Phi_{sol} = 0$ which is opposite behavior to the first model. However, one must recall this model also produces an effective N as well. Similarly the ratio $\log N_{eff} / \log N$ is always greater than 1 meaning since $N = 125$ is greater than 1, $N_{eff} > N$ and thus the overall $(\chi N)_{eff}$ can be greater than the $\Phi_{sol} = 0$ case. If one goes on to compare these values for $(\chi N)_{eff}$ between the models, the model with parameter α generally has a 1 to 2 times larger $(\chi N)_{eff}$ than the δ and β model. Thus the models do not predict the same $(\chi N)_{eff}$ values, but keep in mind that the second model is empirical and is not expected to be realistic in predicting the effective parameters, simply yielding a very good fit to the L_0/λ versus χ and N data.

Overall, the general conclusion from the data is that inclusion of selective solvents increases χ_{eff} with equally mixed solutions doing so only slightly but as Φ_{sol} because composed more of one species over the other, this effect is enhanced greatly with very large increases in χ_{eff} for large Φ_{sol}. An exact quantitative prediction is not possible because the fits above $\Phi_{sol} > 0.20$ start to get progressively worse, as well as the fact that more macrophase segregation is expected in this regime for A only solvent as opposed to the A and B mixed case where phase segregation does not start to dominate until around $\Phi_{sol} > 0.40$.
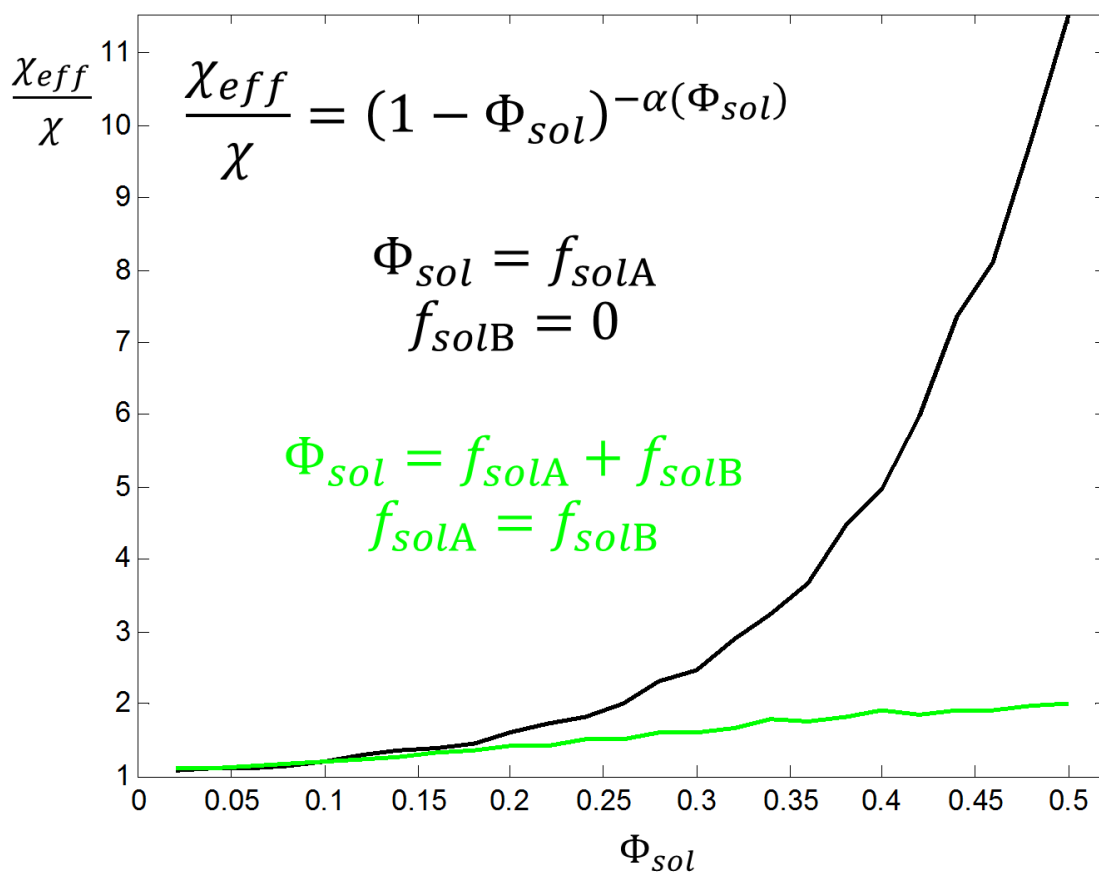
Figure S35: Plot of χ_{eff} normalized by χ versus Φ_{sol} for the model where α was fitted using δ_0 and β_0 from the implicit model (the standard BCP model). Black curve is for the case of A solvent only incorporated into the system and green curve is for the case of equal amounts of A and B selective solvents.
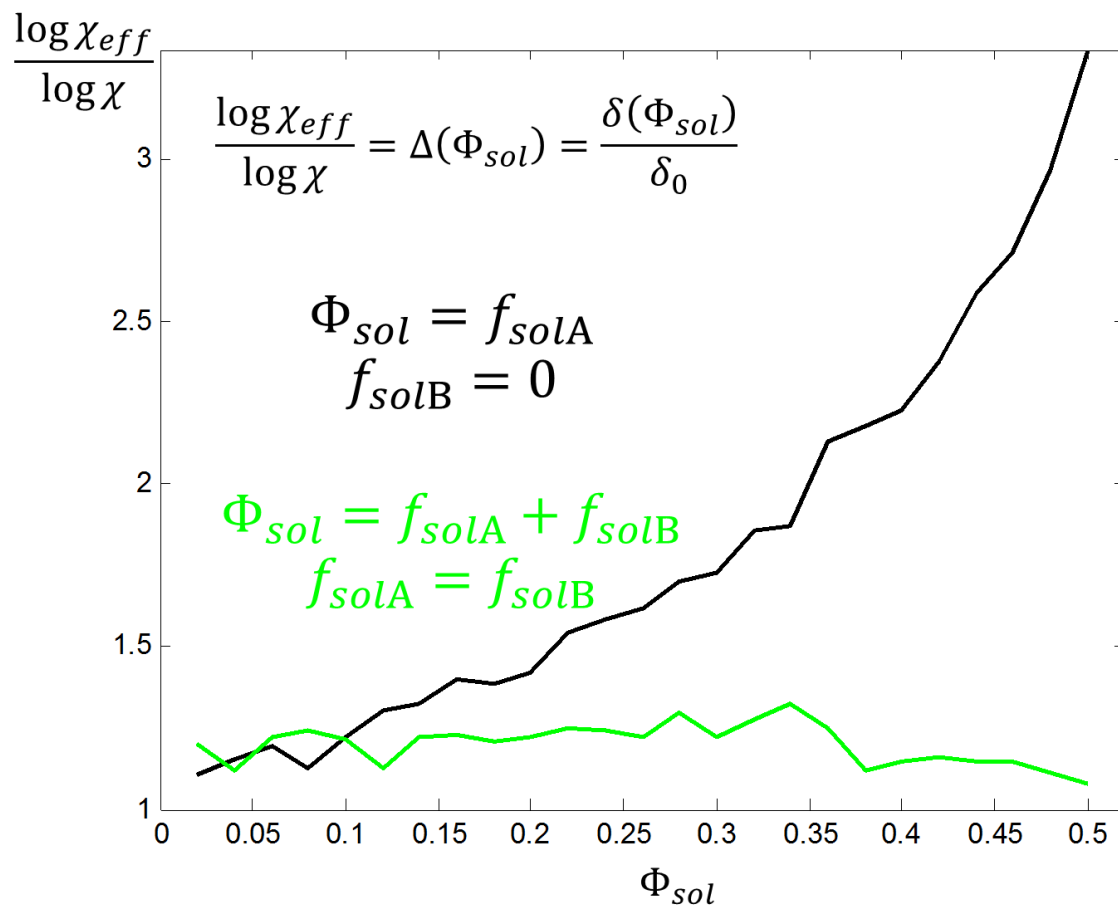
Figure S36: Plot of $\log \chi_{eff}$ normalized by $\log \chi$ versus Φ_{sol} for the model where δ and β were both fitted as a function of Φ_{sol}. Black curve is for the case of A solvent only incorporated into the system and green curve is for the case of equal amounts of A and B selective solvents.

Figure S37: Plot of $\log N_{eff}$ normalized by $\log N$ versus Φ_{sol} for the model where δ and β were both fitted as a function of Φ_{sol}. Black curve is for the case of A solvent only incorporated into the system and green curve is for the case of equal amounts of A and B selective solvents.
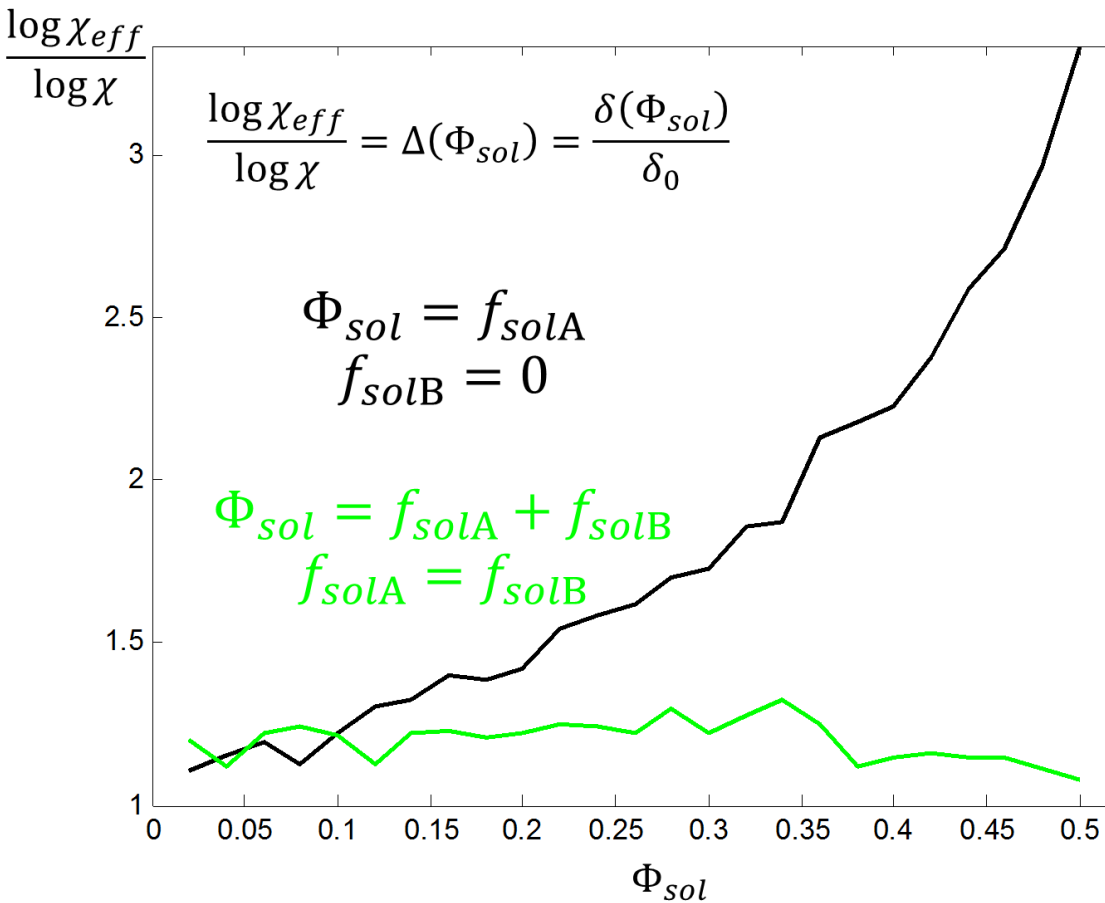
S10: Comparison of Implicit and Explicit Models – 1D Density Profiles

  To compare the density profiles for the implicit model, two density profiles were chosen and plotted side by side in Figure S38 such that $(\chi N)_{eff}$ for the explicit case equals the χN for the implicit simulation. In the plots, the explicit simulation shows the densities of both the BCP species densities, solvent densities, total densities of A solvent and BCP and B solvent and BCP, and overall total density. The implicit simulation only shows the overall A species and B species density since this corresponds to just the BCP in the implicit simulation. As seen at these conditions for $\chi N = 20$ for the implicit case and $\chi N = 12 \rightarrow (\chi N)_{eff} \cong 20$ for $\Phi_{sol} = 0.28$ for equal A and B solvent incorporated, the total species density profiles in the explicit case do appear to have similar shape at these conditions to the implicit model profiles. This gives credence to the implicit model being valid for at least explicit solvent cases, though further work

should be done to validate the model with various degrees of solvent with different selectivity which would require comparison with a four component model, beyond the scope of the present manuscript.
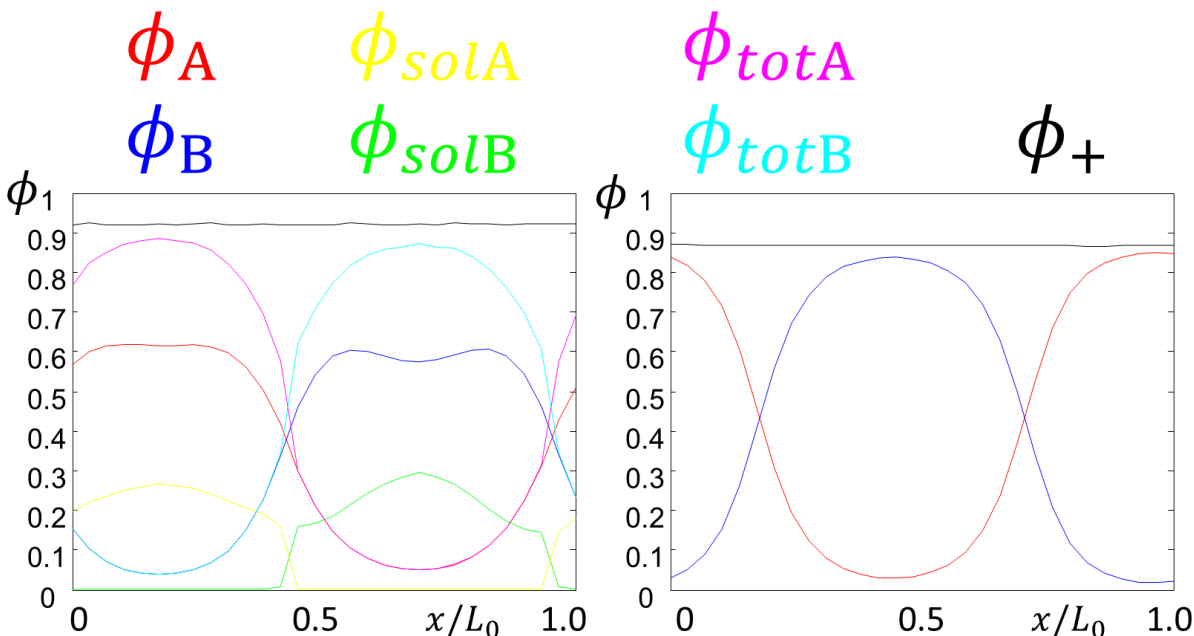

Figure S38: Plots of 1D ϕ density profiles as a function of normalized simulation cell position x/L_0 for (Left) explicit model with equal amounts A and B selective solvents with $\chi N = 12 \rightarrow (\chi N)_{eff} = 20$ and $\Phi_{sol} = 0.28$ and (Right) implicit model with $\chi N = 20$. In both cases $f = f_{eff} = 0.5$. (Left) The explicit model has 7 density profiles plotted over a space of $L = L_0$. Yellow curve is ϕ_{solA}, green curve is ϕ_{solB}, red curve is ϕ_A for the A polymer, blue curve is ϕ_B for the B polymer, magenta curve is the total of the two A species ϕ_{totA} (solvent and polymer), cyan curve is the total for the two B species ϕ_{totB} (solvent and polymer), and black line is the total overall density ϕ_+. (Right) The implicit model has 3 density profiles plotted over a space of $L = L_0$. Red curve is ϕ_A, blue curve is ϕ_B, and the black curve is the total density ϕ_+. Comparing the two plots, the blue curve in the implicit model matches well with the cyan curve in the explicit model as too does the implicit model red curve with the explicit model magenta curve.

S11: Additional Explicit Quasi-Static SVA Simulations

Besides traditional equilibrium structure SCFT simulations, quasi-static simulations were performed where solutions from a given film thickness were seeded into another simulation with a new film thickness and solvent fraction explicitly added to represent incremental swelling. In these simulations, a range of volume fractions $f = 0.3$ to 0.5 were examined with a fixed $(\chi N)_{eff} = 14$. The initial grid size in these simulations was N_X by N_Y by $N_Z = 34$ by 20 by 16 points. The side lengths in these simulations were given values of $2\sqrt{3}L_0$ by $2L_0$ by $1.6L_0$ to bias the simulations to form planar hexagonally close packed structures to specifically investigate the swelling behavior of such morphologies. An initial set of bulk simulations with full periodic

boundary conditions in all three directions were performed to ensure bulk canonical BCP morphologies were observed. As shown in Figure S39, a transition from spheres to cylinders to gyroid to mixed lamellae structures was indeed observed and consistent with previous block copolymer thermodynamic phase diagrams[3]. Pure lamellae were not observed due to metastable mixing of different commensurate lamellae in the non-cubic unit cell.

$f = 0.32$ $f = 0.36$ $f = 0.38$ $f = 0.40$ $f = 0.50$

$\chi N = 14$ L_X by L_Y by $L_Z = 2\sqrt{3}L_0$ by $2L_0$ by $1.6L_0$

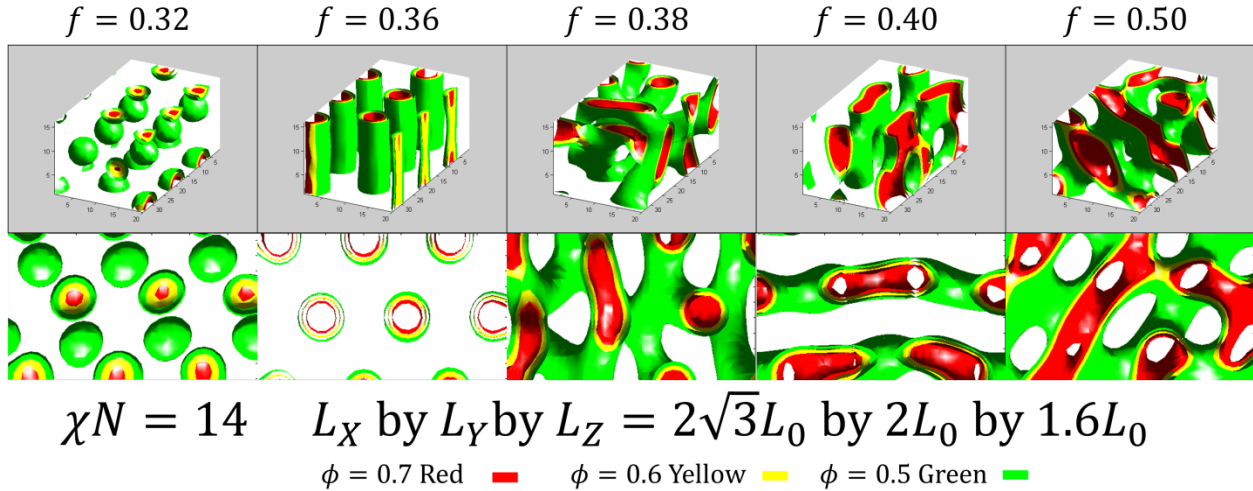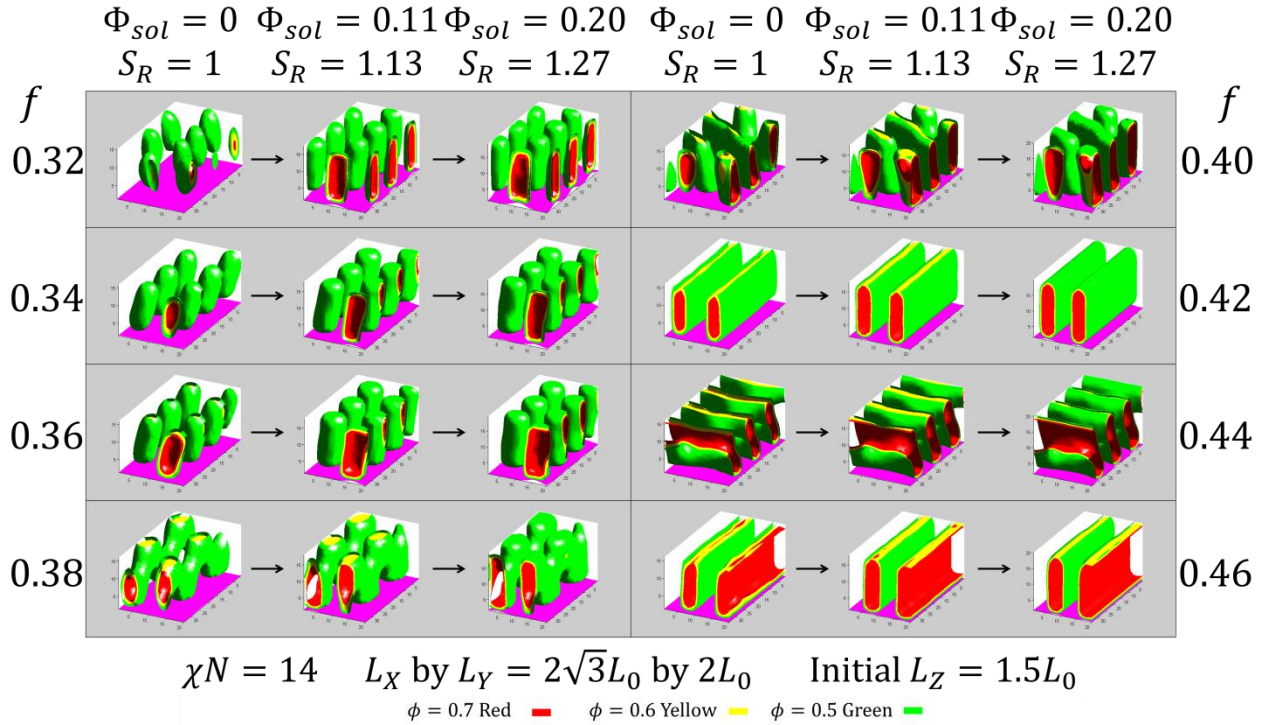$\phi = 0.7$ Red $\phi = 0.6$ Yellow $\phi = 0.5$ Green

Figure S39: SCFT simulation results using bulk full periodic boundary conditions. Upper panels: 3D side view; Lower panels: a top down view. (Left) Hexagonally close-packed spheres. (Middle Left) Hexagonally close-packed cylinders. (Middle) strained gyroid. (Middle Right) Perforated lamellae. (Right) Mixed lamellae.

From the bulk simulation results, various corresponding thin film simulations with different surface energy conditions, and quasi-static swelling simulations, were performed. For each quasi-static swelling simulation, the result of the previous slightly thinner film was seeded into a unit cell 2 grid points thicker, and equal amounts of PS and PDMS preferential solvent were added to the system. The simplest case, shown in Figure S40, had neutral top and bottom surfaces and show that as solvent is added to the system the microdomains become enriched in solvent and extended in the vertical direction. In all these cases, the initial film thickness was $1.5L_0$.

Figure S40: Various quasi-static thin film simulation results with neutral surface boundary conditions. Perpendicular cylinders were observed for $f = 0.32$ to 0.36. Perpendicular perforated lamellae were observed for $f = 0.38$ to 0.40. Perpendicular lamellae were observed for $f = 0.42$ to 0.46.

ESI References

1   W. Bai, A. F. Hannon, K. W. Gotrik, H. K. Choi, K. Aissou, G. Liontos, K. Ntetsikas, A. Alexander-Katz, A. Avgeropoulos and C. A. Ross, *Macromolecules*, 2014, **47**, 6000–6008.

2   H. Elbs and G. Krausch, *Polymer*, 2004, **45**, 7935–7942.

3   M. Matsen and M. Schick, *Phys. Rev. Lett.*, 1994, **72**, 2660–2663.

4   G. Fredrickson, *The Equilibrium Theory of Inhomogeneous Polymers*, Oxford University Press, Oxford, New York, 2005.

5   G. H. Fredrickson, V. Ganesan and F. Drolet, *Macromolecules*, 2002, **35**, 16–39.

6   A. Alexander-Katz and G. H. Fredrickson, *Macromolecules*, 2007, **40**, 4075–4087.

7   A. Alexander-Katz, A. G. Moreira and G. H. Fredrickson, *J. Chem. Phys.*, 2003, **118**, 9030–9036.

8   R. A. Mickiewicz, J. K. W. Yang, A. F. Hannon, Y. Jung, A. Alexander-Katz, K. K. Berggren and C. A. Ross, *Macromolecules*, 2010, **43**, 8290–8295.

9   A. Tavakkoli K. G., K. W. Gotrik, A. F. Hannon, A. Alexander-Katz, C. A. Ross and K. K. Berggren, *Science*, 2012, **336**, 1294–1298.

10   K. W. Gotrik, A. F. Hannon, J. G. Son, B. Keller, A. Alexander-Katz and C. A. Ross, *ACS Nano*, 2012, **6**, 8052–8059.

11   C. Saez, A. Compostizo, R. G. Rubio, A. C. Colin and M. D. Peiia, *J. Chem. Soc. Faraday Trans. 1 Phys. Chem. Condens. Phases*, 1986, **82**, 1839–1852.

12   W. Li, M. Liu, F. Qiu and A.-C. Shi, *J. Phys. Chem. B*, 2013, **117**, 5280–5288.

13   F. S. Bates and G. H. Fredrickson, *Annu. Rev. Phys. Chem.*, 1990, **41**, 525–557.